Journal of Energy Chemistry 76 (2023) 90–104

Contents lists available at ScienceDirect

Journal of Energy Chemistry

journal homepage: www.elsevier.com/locate/jechem

http://www.journals.elsevier.com/journal-of-energy-chemistry/

Review

MXene terminating groups =O, –F or –OH, –F or =O, –OH, –F, or =O, –OH, –Cl?

Tariq Bashir, Sara Adeeba Ismail, Jiaqi Wang, Wenhao Zhu, Jianqing Zhao *, Lijun Gao *

College of Energy, Soochow Institute for Energy and Materials Innovations, Soochow University, Suzhou 215006, Jiangsu, China

ARTICLE INFO

Article history:
Received 24 February 2022
Revised 20 August 2022
Accepted 22 August 2022
Available online 28 August 2022

Keywords:
MXene surface terminating groups
Characterization
Conductivity
Oxidation

ABSTRACT

MXenes are a novel family of two-dimensional (2D) materials that are fast gaining popularity due to their versatile characteristics. The surfaces of these materials are often functionalized by negatively charged terminal groups, such as =O, OH, and F during their synthesis, and it has been hypothesized that regulating the surface terminators enables to control the material characteristics. However, there is still a large gap between computational and experimental investigations regarding comprehending the surface functional groups. Surfaces with mixed terminations are consistently synthesized in experiments, although pure terminated surfaces are predicted by computational research. Here we summarized the nature of chemical bonding in transition metal carbide materials (MXenes) by ^1H and ^{19}F nuclear magnetic resonance (NMR), Raman, X-ray absorption near edge structure (XANES), extended X-ray absorption fine structure (EXAFS), ultraviolet photoelectron spectroscopy (UPS), X-ray photoelectron spectroscopy (XPS)/scanning transmission electron microscopy (STEM), and thermogravimetric analysis-mass spectrometry (TGA-MS) characterizations. Previous literature reveals that =O, –OH, –F, and –Cl are typical MXene surface terminators. However, recent comparative investigations on the valence band intensity distribution in MXenes reveal that the –OH cannot be considered an intrinsic termination species in MXenes. The surface terminals (=O, –OH, –F, and –Cl) of several MXenes, particularly V_2CT_x and $Ti_3C_2T_x$, will be identified and quantified here. We have also discussed different etching approaches for the synthesis of MXene, the dependence of MXene conductivity on MXene terminating groups, and the emission of various gaseous products that evolved during its chemical transformations. This paper provides significance, especially in the field of energy conversion and storage materials, where the intercalation process is crucial.

1. Introduction

MXenes are two-dimensional (2D) transition metal carbides and nitrides [1–3] that have gleaned attention as electrode materials in lithium-ion batteries (LIBs) [4–6], Li-S batteries [7,8], sodium-ion batteries (SIBs) [9,10], catalysts [11,12], supercapacitors [13–15], etc. MXenes are synthesized by etching out the element 'A' from the MAX phase. $M_{n+1}X_nT_x$ is the generic formula for the MXene family, where M stands for transition metals such as Ti, V, Nb, Mo, Cr, Zr, Mn, Tc, Sc, and so on, X stands for C and/or N, and T_x stands for terminal surface groups such as –F, =O, and/or –OH. For example, an aqueous etching of the Al from the MAX phase (Ti_3AlC_2) does not leave bare Ti layers and produces functional groups (T_x), resulting in $Ti_3C_2T_x$.

The preparation technique and reagent employed for initial MAX phase etching have a large impact on the surface termination of MXene flakes. Generally, HCl/LiF or HF etching permits a change in the relative amounts of –OH, =O, and –F-terminated groups on the MXene surface [16–18]. In several studies, first-principles simulations have revealed a predilection about the termination of bare MXene surface. Many investigations have found that terminating a bare MXene surface is preferable. MXenes have high negative formation energy at surface termination, showing a strong link between the surface terminating groups and the M atoms [19,20]. Pang et al. [21] recently discovered a novel technique for the synthesis of –Cl, –Br, and –I-terminated MXene by etching the "A" layer with molten salt ($ZnCl_2$). They also observed that MXene can be further terminated with –S, –Te, and –NH by addi-

---

* Corresponding authors.
E-mail addresses: jqzhao@suda.edu.cn (J. Zhao), gaolijun@suda.edu.cn (L. Gao).

https://doi.org/10.1016/j.jechem.2022.08.032
2095-4956/

tional chemical modification [22,23]. Terminations also have an impact on energy storage properties. On the atomic scale, first-principles simulations were performed to explore the processes and predict the energy storage characteristics of MXenes. In Li-ion batteries, the theoretical capacities of Ti_3C_2, $Ti_3C_2O_2$, $Ti_3C_2F_2$, and $Ti_3C_2(OH)_2$ were 320, 268, 130, and 76 mAh g^{-1}, respectively [3,24,25]. Recently, Li et al. [26] synthesized –Cl-terminated Ti_3C_2 MXene using a molten salt synthesis technique, which delivers a Li^+ storage specific capacity of 205 mAh g^{-1} with high charge–discharge rate. Li et al. [27] used Lewis acidic-melt etching technique to synthesize $Ti_3C_2T_x$ MXenes with –Cl, –Br, –I, –ClBr, –ClI, –BrI, and –ClBrI halogen terminating species. The synthesized halogenated MXene ($Ti_3C_2(OF)$ were used in zinc-ion battery cathode material. The discharge capacity of unitary-halogen-terminated $Ti_3C_2I_2$ and $Ti_3C_2Br_2$ is around 1.1 and 1.6 V, with specific capacities of 135 and 97.6 mAh g^{-1}, respectively. The dual discharge capacity of multi-halogen-terminated $Ti_3C_2(ClBrI)$ and $Ti_3C_2(BrI)$ have specific capacities of 107.4 and 117.2 mAh g^{-1}, respectively. In contrast, without a platform, $Ti_3C_2(OF)$ and $Ti_3C_2Cl_2$ have specific capacities of 51.75 and 46.5 mAh g^{-1}, respectively. MXene etched with molten salt (MS-$Ti_3C_2T_x$) lacks –OH termination. Li et al. [26] stated that MXenes synthesized by the molten salt synthesis have an enhanced Li^+ storage capacity of 205 mAh g^{-1} with a high charge–discharge capacity and rate performance for electrochemical energy storage applications. Xie et al. [3] presented DFT calculations showing reduced adsorption energy of Li ion on MXenes terminated with the dominant =O terminator compared to the surface –OH–terminated MXene materials, resulting in greater interaction between Li and =O and enhanced Li storage capacity. As a consequence, $Ti_3C_2T_x$ MXene with a high proportion of the =O terminator is expected to the capacity increase for lithium storage. The volumetric capacitance of oxygen concentration and the lack of –OH terminating groups of MS-$Ti_3C_2T_x$ films has also been demonstrated to be improved by surface modification [28,29]. As Ti–F bonds became unstable in the basic solution, it was discovered that the alkalinizing process caused –F terminating groups to be preferentially replaced by readily removable –OH [3,30]. Liu et al. [31] fabricated surface-modified $Ti_3C_2T_x$ films through alkalization (ak-$Ti_3C_2T_x$). The annealing treatment boost the crystalline order of $Ti_3C_2T_x$ samples, remove surface groups and enhance exposed redox-active sites [32]. Recently, it has been pointed out that the properties of MXenes are primarily controlled by its surface terminators [33–36], and it is necessary to assume average site occupancy of functional groups, such as by analyzing the paired distribution function [37], or simply by using a type of complete termination assumed in density functional theory (DFT) calculations [2,3,5,25].

The DFT analysis also indicated that surface terminal groups have a substantial effect on the electron band occupancy [38] and work function [39] of MXenes, which has to be validated by experiments. According to previous DFT research, terminating $Ti_3C_2T_x$ and Ti_3CNT_x with –OH, –F, and/or =O considerably changes the electronic states around EF [2,24,40–42]. The DFT predicts a local maximum in the density of state (DOS) at EF for non-terminated $Ti_3C_2T_x$ and Ti_3CNT_x, however, the DOS(EF) is drastically lowered when the surface is completely functionalized. As a result, by lowering the carrier concentration, surface functionalization may change the electrical resistance. DFT analysis also suggested that the performance of MXenes in LIBs [3,25], SIBs [43,44], catalysts [45,46], supercapacitors [47,48], and the electronic characteristics are strongly reliant on surface functionalization, implying that surface terminating group preference and study are critical. DFT calculations by Khazaei et al. [39] demonstrate that –OH-terminated MXenes achieve ultralow work function regardless of the kind of M element. Li et al. [49] also suggest that the S-doped mesoporous structure provides a large active surface area and quick electron transfer for the Faradaic process involving surface or near-surface redox reactions. In addition, it was observed that the increase or decrease in the working functions of MXenes upon –F or =O functionalization depends on the type of M element. As a result, a greater understanding of the surface functionalization of these fascinating materials will assist in the development of new applications.

Therefore, it is crucial to accurately characterize the surface terminators of MXenes due to their critical roles in their properties. The chemical characteristics of surface terminators in MXenes have been studied using a variety of methods, including UPS/XPS, XPS/STEM, XANES, EXAFS, ^1H, and ^{19}F NMR spectra. However, XPS remains the most frequently utilized of all technologies. Using XPS to analyze MXenes has numerous advantages, including the fact that it is sensitive to all elements except H and He [50]. It can be used to examine elemental composition (including termination) and constituent elements bonding environments and can detect tiny quantities of elements, particularly on the surface [50–53]. The importance and proper understanding of the bonding conditions of MXene surfaces has been demonstrated by many theoretical and experimental studies.

In this review, we studied the termination groups of various MXenes investigated so far. ^1H and ^{19}F NMR, XANES, EXAFS, Raman, XPS fitting models and TGA were used to examine the coordination of the adsorbed surface terminating groups, i.e., (T_x species). We argue that terminating =O and –F has more fitting ambiguity than terminating –OH and –F in high-resolution spectra. There is much evidence in the previous literature about –OH terminating groups on MXene surface, however, there is ambiguity about the –OH terminating group in the recently published literature, therefore, it is critical to investigate the presence of –OH, =O, or both of the groups, as well as –F on the MXene surface as a terminating group. Different approaches towards the synthesis of MXenes, the influence of MXene conductivity on MXene termination groups, and gases synthesized during its chemical transformations have also been explored here.

2. Different approaches towards the synthesis of MXenes

Clean and green chemistry synthesis should be considered while synthesizing MXene from the MAX phase. The comparative studies of fluoride etching, electrochemical etching, water-free etching, and alkali treatment that have all been used to synthesize MXenes are listed below.

2.1. Fluoride etching

Fluoride etching can be accomplished in two commonly-used methods. One method is to use concentrated HF to etch directly on MXene surface. MXenes with multilayer architectures are exfoliated by sonicating in isopropyl alcohol and methanol after the MAX phase has been etched at room temperature. The other one is in-situ [54] synthesis of HF from HCl and fluorides, including CsF [55], FeF_3 [56], NaF [57], CaF [55], LiF [55], KF [56], and tetra-n-butyl ammonium [55]. The synthesis of MXenes has been reported by Naguib et al. [2] described the chemical interaction between the MAX phase and the fluorine-based aqueous solution in which MXenes are synthesized. The MXenes were terminated with –F and –OH after the removal of Al atoms, however, the oxygen termination was also observed. Ti-O, Ti-OH, and Ti-F were used to replace the Ti-Al position. Various MXenes such as Ti_3CNT_x [58], $TiNbCT_x$ [18], Nb_2CT_x [59], $Mo_2Ti_2C_3T_x$ [60], TiC_2T_x [7], $Ti_3C_2T_x$ [61], $(Nb_{0.8}Zr_{0.2})_4C_3T_x$ [62], $(Nb_{0.8}Ti_{0.2})_4C_3T_x$ [62], and $Zr_3C_2T_x$ [63] were effectively synthesized using this approach. Fluorine-based solutions or direct HF etching has been effectively used in the synthesis of MXenes and has since become a common preparation procedure. However, this approach has some drawbacks, including the fact that Al atoms in MAX phase precursors have a strong reactivity with F and fluoride-based aqueous solutions are only effective for Al-containing MAX-phase precursors, which limits the synthesis of MXene from non-Al MAX phase precursors. When the HF is used, it causes environmental and safety issues. The F-terminal groups also limit material performance, preventing MXenes from being used in new applications. To summarize, developing novel HF-free etching methods is critical.

2.2. Electrochemical etching

The reactivity differential between the M–Al and MM–C bonds is the basis for chemical etching. Electrochemical etching, on the other hand, is the process of transferring a charge. Sun et al. [64] showed that electrochemical extraction of Al on porous Ti_2AlC electrodes in diluted HCl solution was effective. Ti_2AlC can be used to synthesize a layer Ti_2CT_x MXenes. Unlike chemical etching with LiF/HCl or HF, electrochemical etching did not use any F ions, yielding MXenes with just –Cl, =O, and –OH groups. The over-etching of the MAX phase into carbines-derived carbon (CDC) might be due to the problem of electrochemical etching. The electrochemical etching of Ti_2AlC to CDC and Ti_2CT_x was explained using a core–shell model. It proposed that to make MXenes without overloading, etching conditions should be properly controlled. Electrochemical etching has broadened the MXene composition prospects and scope of etching methods. Yang et al. [65] showed that electrochemical corrosion may be used to synthesize $Ti_3C_2T_x$ MXenes. Al atoms can be precisely replaced with –OH groups by changing the electrolyte composition. As a result, double-layer or single-layer $Ti_3C_2T_x$ nanosheets with a large size yield of more than 90% may be synthesized. Thermochemical etching with heat assistance has been described [21]. Ti_2CT_x, V_2CT_x, and Cr_2CT_x are three MXenes samples synthesized without the use of HF. Gentle heating accelerates the etching process of the MAX phase in the presence of diluted HCl as an etchant, hence considerably increasing the etching efficacy of MXenes. Thermal-assisted electrochemical etching not only presented a universal technique for MXene synthesis, but it has also synthesized MXenes that were previously difficult to synthesize. It opens up a new window for the synthesis of MXenes in a safe, rapid, and facile way.

2.3. Water-free etching

Molten salt etching (Lewis's acid etching) and iodine aided etching are the two most used non-aqueous etching procedures. In molten salt (Lewis acid), MAX phase reactions were comparable to those in the HF, such as Ti_3AlC_2 in molten $ZnCl_2$ [22]. By increasing the ratio of MAX: $ZnCl_2$, the Ti_3ZnC_2 MAX phase was attained, which was subsequently converted into $Ti_3C_2Cl_2$ MXenes. Following the optimization of the procedure, $M_{n+1}Z_nX_n$ phases were produced by substitution, yielding consistent MXenes ($M_{n+1}X_nCl_2$) with a Cl group on the surface. Li et al. [26] synthesized of MXenes using molten Lewis acid in 2019 conducted an in-depth and systematic investigation and presented the technique of preparing MXenes using universal molten salt. Lewis's acid cations had such a high redox potential that they can easily oxidize the A atoms in the MAX phase. A variety of molten salts ($NiCl_2$, $AgCl_2$, $CuCl_2$, $CoCl_2$, $FeCl_2$, $CdCl_2$) were used to etch distinct MAX phases (Ti_3AlCN, Ti_2AlC, Nb_2AlC, Ti_3AlC_2, Ta_2AlC, Ti_2ZnC, Ti_3ZnC_2) to produce the matching MXenes under the direction of this redox potential-based rule. These findings showed that the late transition metal halide may be used to replace A atoms in the typical MAX phase. It has substantially extended the range of MAX phases that may be used as MXene precursors. Lewis acid etching is a practical and green approach for producing MXenes since it does not need the use of HF. Shi et al. [66] recently stated non-aqueous iodine (I_2) assisted etching technique for 2D MXene with rich oxygen terminating groups. The $Ti_3C_2I_x$ was synthesized by I_2 etching in anhydrous acetonitrile at 100 °C, then stratified in HCl solution to further change $Ti_3C_2I_x$ into $Ti_3C_2T_x$ films of moderate size.

2.4. Alkali etching

Alkali is perfect for etching MAX phase Ti_3AlC_2 due to its high reactivity with Al. The challenge in producing MXenes by alkali etching lies in reaction kinetics since certain oxides/hydroxides will develop on the surface of Ti_3AlC_2 [67–69]. KOH was successfully used as an etching agent for the synthesis of MXenes by Li et al. [68], and a single-layer $Ti_3C_2(OH)_2$ were successfully etched. However, alkali exposure can lead to the production of Al oxide/hydroxide layers such AlO(OH) and $Al(OH)_3$, which can obstruct the desired Al removal. Only the Al atoms from the outer surface of MAX phase Ti_3AlC_2 were removed in Xie's work [67]. Furthermore, while the alkali treatment eliminated some of the Al, Zou et al. [70] found that certain Na/K-Ti-O compounds were formed instead of MXene. As a result, these oxidation layers must be eliminated. The preparation of $Ti_3C_2T_x$ (T = OH and/or O) was reported using NaOH-assisted hydrothermal etching of Ti_3AlC_2 [69]. To prevent the material from oxidizing, this hydrothermal treatment was performed in an argon environment. By selectively removing Al from Ti_3AlC_2 using NaOH solution at 270 °C, the multilayer $Ti_3C_2T_x$ was synthesized. Without visible F terminal groups, the purity of the material containing =O and –OH terminal groups were 92 wt%. The acidic or amphoteric atoms of the MAX phase were successfully removed using the alkali etching approach. It offers an HF-free approach to fabricate novel MXenes.

3. The ambiguity of surface terminating group (O or –OH?)

Based on the above discussion, it is critical to gain deep insight into MXene surface terminal groups. It is possible to change the properties of MXenes by changing the surface group. However, the study of =O and –OH surface terminating groups is limited; therefore, it is critical to study the preferences and environment of MXene surface functional groups.

3.1. NMR study

NMR is a powerful technique for examining fluorine and hydrogen-containing materials because of the great sensitivity of –OH, =O, ^1H, and ^{19}F nuclei [71]. Hope et al. [35] studied MXene functional groups using NMR and observed corresponding ^{13}C NMR data (Fig. 1a), which shows that Ti_3AlC_2 to $Ti_3C_2T_x$ has been converted. V_2AlC and V_2CT_x have chemical shifts of 208 and 265 ppm, respectively, compared to $Ti_3C_2T_x$ (382 ppm). The original ^1H NMR experiment revealed that only H_2O caused significant resonance at 6.9 ppm; however, after drying at 200 °C in a vacuum oven overnight, distinct proton environments could be differentiated (Fig. 1b). HF-synthesized MXene has a broad signal (18.6 ppm), which is comparable to that of LiF-HCl-synthesized MXene (12.5 ppm). The terminations with various degrees of hydrogen bonding are assigned to –OH. The two ^1H spectra also have a 6.5 ppm characteristic, which is attributed to H_2O, since its intensity is sensitive to the degree of drying, suggesting that vacuum drying at 200 °C cannot entirely remove the water trapped between the layers of MXene. 2D ^1H–^{13}C heteronuclear correlation (HETCOR) spectra of HF synthetic samples were collected to validate the connection of the –OH group to the $Ti_3C_2T_x$ sheet (Fig. 1c). These tests indicate that an angstrom correlation exists only between species that are very close in proximity [72]. Although the spectrum is broad, the –OH terminations at δ ^{1}H ~20 ppm are associated with the $Ti_3C_2T_x$ carbon environment at δ ^{13}C ~380 ppm, confirming the connectivity. There are no further ^{1}H signals in this spectrum, suggesting that the environment is far away from the carbon layer and/or highly mobile, i.e., intercalants, as opposed to surface terminating species. The significant ^{1}H chemical shift outside the typical ^{1}H chemical shift range in these systems might be due to one of three main reasons: transmitted hyperfine (or Fermi contact) displacement because of the Ti layer unpaired spin density transformation; Knight shift owing to metal behavior; and/or strong H-bonding. Previous NMR investigations of V_2CT_x discovered that the –OH termination exhibited higher ^{1}H chemical shifts (85 ppm), which were attributable to the knight shift generated by metal V_2CT_x with a short band gap [73].

The T1 relaxation constant of the –OH signal is ~3 s, and the hyperfine interaction should produce rapid T1 relaxation, according to the ^{1}H saturation recovery experiment on $Ti_3C_2T_x$; by comparison, the T1 relaxation constant of the –OH termination in V_2CT_x is ~1 ms. In addition, Hope et al. [35] conducted a variable temperature ^{1}H NMR experiment. There was no substantial difference in the chemical shift or hyperfine shift between −8 and 62 °C. Therefore, the substantial chemical shift of the –OH terminations in $Ti_3C_2T_x$ is due to a strong hydrogen bond rather than a hyperfine shift. In the two different samples, two different hydrogen bond configurations were observed. However, the small contribution of the knight shift cannot be excluded, especially because the observed chemical shift is near the maximum ^{1}H shift observed in strong hydrogen bonding systems, and the ^{13}C NMR spectrum shows a large shift that could be due to the Knight shift in $Ti_3C_2T_x$. Wide signals were observed for the ^{19}F spectra (Fig. 1d), which were characterized as –F termination, at −227 ppm in HF synthetic samples and −255 ppm in LiF-HCl synthetic samples. There is resonance at 8 ppm in the LiF-HCl manufactured samples, which is most likely due to TiF_3 synthesized under more severe etching conditions, and a broad signal at −100 ppm, which might be attributable to metal oxyfluoride pollution or fluorinated hydrocarbons. ^{1}H-^{19}F HETCOR spectra were also recorded to investigate the spatial organization of various functional groups, as shown in Fig. 1 (e and f). The correlation between –F and –OH terminations in both samples showed that there were mixed terminations in the layer rather than regions terminated by a single functional group, thus confirming the spectral distribution. The presence of structural H_2O molecules between MXene nanosheets is indicated by the substantial connection between H_2O and –F termination; the low mobility of H_2O molecules may suggest a strong correlation, but this needs to be validated by additional experiments at varied contact periods.

3.2. Raman study

Raman spectroscopy is a powerful technique used to study two-dimensional materials. Despite the fact that MXenes is a vast 2D transition metal nitrides and carbides family, there has been very little Raman research on it. Partial phonon density of states, phonon dispersion, Raman, and infrared active vibration have all been predicted for the $Ti_3C_2T_x$ monolayer lattice [74]. According to Hu et al. [75], the surface group T_x has been affected by lattice vibration. Furthermore, experiments were carried out utilizing these estimates for peak distribution and analyzing data during field electrochemical measurements. They demonstrated how the peaks corresponding to the –O(OH), –(OH), and =O groups altered throughout the electrochemical cycle. The experimental results indicate that the mixed terminations (=O and –OH) should be incorporated in the MXene structure calculation model. The Raman spectra of $Ti_3C_2T_x$ are also known to be influenced by plasmonic characteristics. The $Ti_3C_2T_x$ resonance peak arises at 120 cm^{-1} when the laser wavelength is resonantly associated with the plasmon resonance. The Raman spectrum of $Ti_3C_2T_x$ film may be affected by the preparation process, as stated by Lioi et al. [76], indicating that the Raman spectrum may be utilized to monitor the quality change of MXene as a function of synthesis parameters. Finally, Raman spectra from 6 nm thick MXene films were obtained, but no single-layer MXene spectra were found. As shown in Fig. 2(a), the MXene Raman spectra may be separated

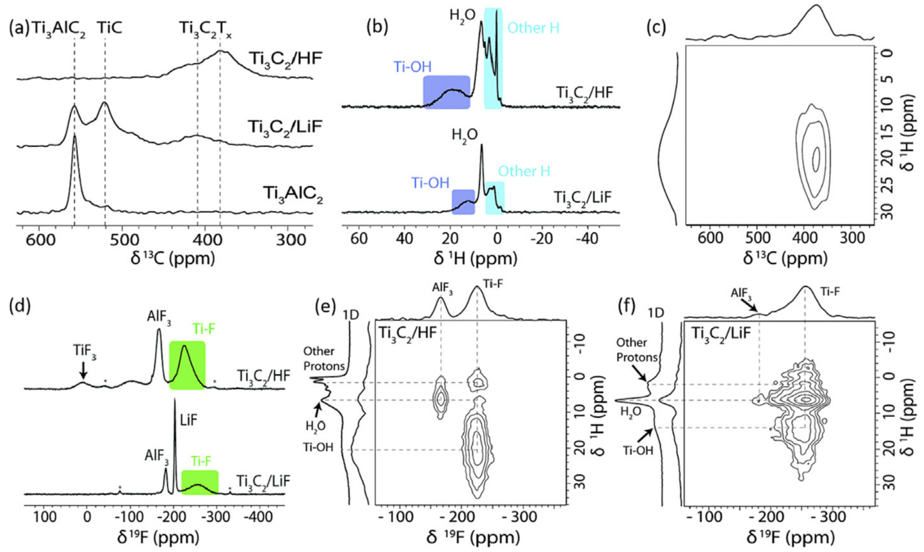

Fig. 1. (a) ^{13}C NMR (11.7 T) spectra of $Ti_3C_2T_x$ and Ti_3AlC_2 synthesized by two different methods, recorded at 50 kHz MAS using a carr-purcell-meiboom-gill (CPMG) method, with the echo sum to obtain the conventional line shape. (b) ^{1}H NMR (11.7 T) spectra of $Ti_3C_2T_x$ MXene synthesized in LiF + HCl and HF, measured at 60 kHz MAS. (c) ^{1}H–^{13}C HETCOR NMR (7.05 T) spectrum of HF-synthesized $Ti_3C_2T_x$ MXene measured at 40 kHz MAS. (d) ^{19}F NMR (11.7 T) spectra of HF- and LiF-HCl-synthesized Ti_3C_2 MXene measured at 60 kHz MAS. ^{1}H-^{19}F HETCOR NMR (11.7 T) spectra of (e) HF and (f) $Ti_3C_2T_x$ MXene synthesized by LiF + HCl recorded at 20 kHz MAS were compared with adjacent ^{1}D ^{1}H spectra. Reproduced with permission from ref. [35]. Copyright 2016. Communication (RSC) publishing group.

into several regions. When a 785 nm laser is utilized, the resonant peak is seen to be associated with the plasmonic peak [75]. The flakes region consists of A1g (Ti, C, O) and Eg (Ti, C, O) modes, which are the out-of-plane and in-plane vibrations of titanium and carbon atoms as well as surface terminators in the outer layer, which shows that group vibration of Ti and C atoms as well as surface terminator groups cause flakes vibration. This vibration is the most difficult since it includes the most atoms from MXene. Furthermore, the ranges 230–470 cm^{-1} indicate in-plane (Eg) vibrations of surface terminators of Ti atoms because only surface atoms affect this region therefore could be utilized to identify changes in MXenes surface chemistry caused by electrochemical or chemical reactions. Carbon vibration is mostly responsible for the area between 580 and 730 cm^{-1} (A1g and Eg). Various in-situ electrochemical experiments have employed the latter region for surface group fingerprinting [77]. Shortly surface groups can be monitored using Raman spectroscopy. The influence of the composition of the etching solution, specifically the HF concentration, on the Raman spectrum of the MXene flakes was extensively examined because the surface chemistry is dependent on the etching procedure, as shown in Fig. 2(a). All of the $Ti_3C_2T_x$ tested had a resonant excitation wavelength of 785 nm. The spectra of multilayer repackaged films were acquired by mapping a patch of 10 μm × 10 μm with an average total of 100 spectra to avoid the influence of roughness. Fig. 2(b–e) depicts the key features of the spectra. The multilayer samples synthesized by etching processes are compared in Fig. 2 (b). It is worth noting that the multilayer sample was created by drying the clay material in the in-situ HF process. $Ti_3C_2T_x$ has intercalated Li-ions but did not delaminate in this case. The multilayer powder and intercalated "clay" synthesized using the HF-HCl technique have comparable spectra. However, both spectra show an increase in the OH component of the surface terminator and the positions of the A1g(C) peaks are similar. The O component of the HF-etched multilayer material, on the other hand, takes precedence, and the A1g(C) peak shifts to 711 cm^{-1}. When HCl is added, the pH rises, resulting in protonated surfaces. The A1g (C) peak position of the multilayer sheets was moved to 730 cm^{-1} by the introduction of TMAOH intermediate after HF etching. The increase in interlayer space induced by intercalant molecules might explain this dramatic shift. As demonstrated in Fig. 2(c), the peak value of A1g (C) downshifts as the HF concentration rises. As the concentration of HF increases, the ratio of A1g (Ti, C, T_x)/A1g(C) decreases. A stronger and sharper peak ofA1g (Ti, C, T_x) suggests a lower sheets rotation relative to each other as well as lower the defect concentration. The multilayer repackaging films produced by etching in LIF/HCl, HF/HCl, and HF were compared to compare different etching procedures (Fig. 2d). Surprisingly, only HF-HCl etching causes the resonance peak to shift. The resonant Raman peak is linked to material vibronic properties, and the electronic properties of MXene may influence its resonant spectrum. The observed peak displacement can be explained in this way. Varied $Ti_3C_2T_x$ synthesis processes affect the surface chemical characteristics and defect concentration, leading to different electronic properties, as is well known [24,79]. The peak shifts of A1g(C) and A1g (Ti, C, O) in LiF/HCl and HF/HCl etching are similar. The significant difference in the Raman spectra of these films, aside from the resonant peak shift, is the shift of the A1g(C) peak. In reality, the contrast between LiF/HCl etched delaminated and "clay" MXene is remarkably comparable, as shown in Fig. 2(e). This suggests that the samples synthesized by the HF/HCl technique and the LiF/HCl approach differ significantly. There is no difference between the flakes of both samples (delaminated and "clay" MXenes) because both samples have a higher intensity of A1g (Ti, C, O). This can be explained by the fact that the flakes in both samples have no registry [78].

3.3. XANES study

Previously, the Ti 1*s* EXAFS and XANES spectra of Ti_3AlC_2 and $Ti_3C_2T_x$ were published [80–82]. Magnuson et al. [36] carried out *K*-edge XANES research and found that MXene had –F and =O terminators. As shown in Fig. 3(a), the Ti 1*s* XANES absorption spectra of Ti metal, TiC, Ti_3AlC_2, and $Ti_3C_2T_x$ have two regions: pre-edge and main edge. Coordination, symmetry, and bond angle are all important factors for the pre-edge features [83]. The weakly interacting Al layer is replaced with the highly interacting termination species T_x, where =O and –F atoms draw charges from Ti, resulting in a 1.4 eV shift of the C peak between the Ti_3AlC_2 and $Ti_3C_2T_x$ spectra [36]. It is also observed that Ti_3AlC_2 and $Ti_3C_2T_x$ EXAFS structure factor oscillations and compared them to Ti metal benchmarks. The Ti–Ti distances of $Ti_3C_2T_x$ (3.016 and 3.072 Å) are somewhat different from the Ti–Ti atomic distances in Ti_3AlC_2 (3.029 and 3.032 Å) shown in Fig. 1(b). The in-plane Ti-Ti distance of $Ti_3C_2T_x$ is 3.016 Å, which is somewhat less than the estimated in-plane Ti-Ti atomic distance determined from the X-ray diffraction (XRD) lattice parameter (a = 3.075 Å) [36]. The overlaying scattering of Ti–O, Ti–F, and Ti–C in the first coordination shell of $Ti_3C_2T_x$ causes peak characteristics between 0 and 2 Å in the first coordination shell, where the Ti–C interaction has two different contributions: Ti-I is used for the internal Ti atom bond only to C, and the contribution of the second Ti-II is used for the external Ti atom bond to C and terminating species. The outer Ti atom Ti–C bond length is 0.056 Å longer than the inner Ti atoms. Furthermore, due to the overlaying scattering of Ti-Ti (such as Ti—C—O, Ti–Ti–C, Ti–C–F, and Ti–F–Ti–F), the three peaks in the higher coordination shell between 3 and 6 Å also contribute significantly to the long inclined single Ti–F and Ti–O scattering paths from all surface Ti atoms to the terminating species T_x [36]. In summary, there is no evidence of –OH terminators in MXene nanosheets based on XANES and EXAFS spectra.

3.4. XPS study

XPS remains the most extensively utilized technology to characterize surface terminal groups due to its numerous benefits regarding analyzing MXenes since it is sensitive to all elements except H and He [50]. It may be used to examine constituent element bonding environments, measure element composition (including termination), and identify minuscule quantities of elements, especially when the elements are on the surface [50]. As an etchant, molten $ZnCl_2$, as a high Lewis acid, may easily exchange the -F-terminated group of MXene with –Cl-terminated MXene. Li et al. [22] successfully synthesized chlorine-terminated Ti_2CCl_2 and $Ti_3C_2Cl_2$ MXenes by selectively etching Ti_2ZnC and $Ti_3Zn_2C_2$ with molten $ZnCl_2$ as the etchant and observed that Cl may be used as a new surface group of MXenes, as shown in Fig. 4(a and b). Qin et al. [84] observed that the mechanical strength of –Cl-terminated MXenes is often lower than that of similar –F-terminated MXenes. The elasticity constant of –Cl-terminated MXenes is often lower than –OH, =O and –F-terminated MXenes, [85] which may be explained by the longer M–Cl bond compared to the M–F and M–O bonds shown in Fig. 4 (c). MXene etched with molten salt lacks both –OH and =O-terminating groups, resulting in limited mechanical stability and conductivity [22,85].

Previous experimental studies using XPS revealed the presence of –OH, =O, and –F terminations [2,4,7], and their proportions were measured using energy-dispersive X-ray spectroscopy (EDS) [2,37,55]. EDS, on the other hand, cannot differentiate between =O and –OH; thus, it is presumed that all =O exists as –OH. Persson et al. [87] concluded that =O and –F occupy the fcc position, –F has priority, and =O can be shifted from the alternative to the fcc

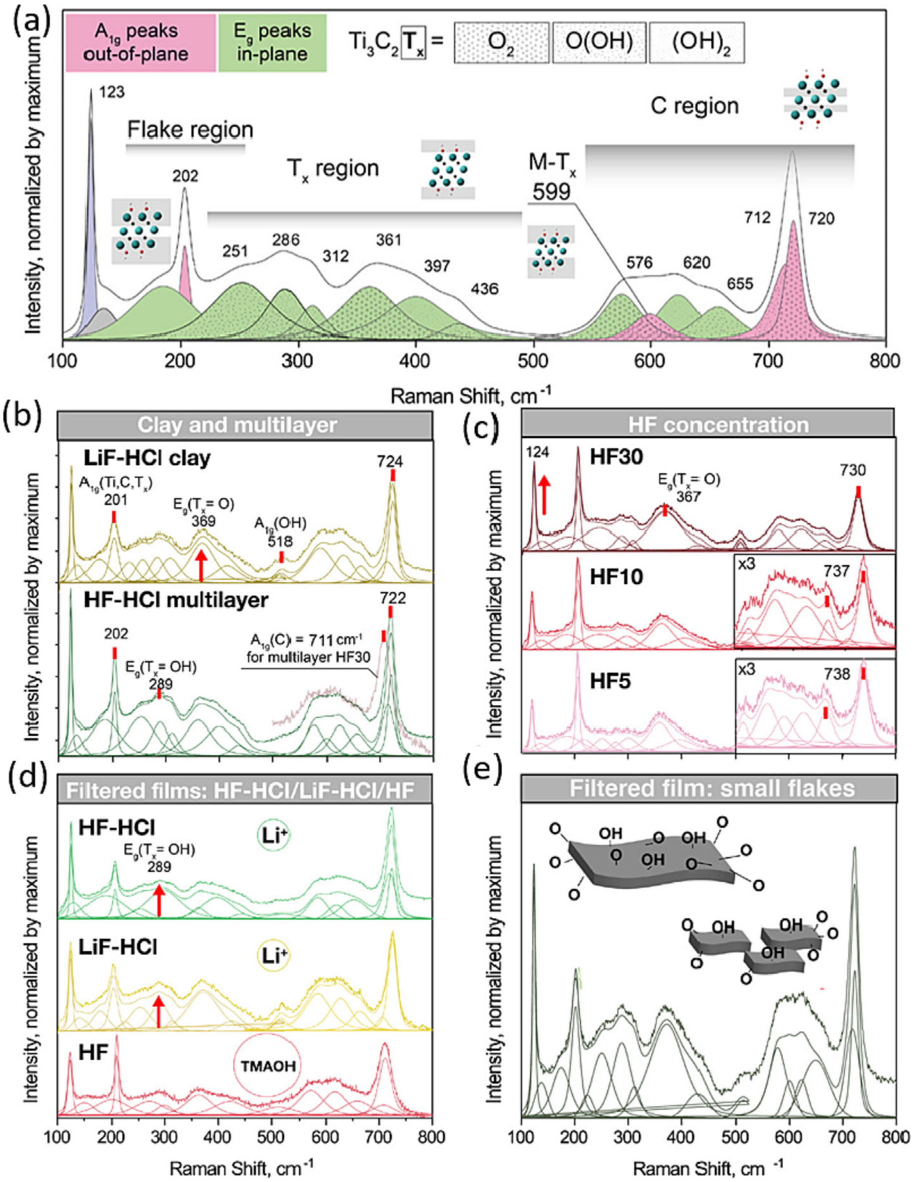

Fig. 2. Effect of intercalants and etching solutions on vibrational modes of $Ti_3C_2T_x$. (a) Deconvoluted Raman spectrum of $Ti_3C_2T_x$ film synthesized by HCl-HF etching and excited by a 785 nm laser was obtained. The spectrum is divided into 3 main regions: (i) The flake region, which is related to vibration of carbon atoms group, (ii) Ti atoms layers and surface terminators, and (iii) the carbon region, which corresponds to the in-plane and out-of-plane vibration of carbon atoms. For each deconvoluted spectrum presented, a matrix of 100 spectra was recorded and averaged. Record the matrix of 100 spectra for each deconvoluted spectrum average and supplied them. In WiRE 3.0 software, using the Voigt function to perform deconvolution. (b) ''Clay'' and multilayer MXenes's Raman spectra. (c) Raman spectra of $Ti_3C_2T_x$ as a function of HF concentration. (d) Effects of various synthesis processes on the parameters of layered vacuum-assisted filter flakes. In the case of LiF-HCl and HCl-HF etching, lithium ions were employed for the delamination process, while in the case of HF etching, TMAOH was used. (e) Raman spectra filtered into the film from 100 nm $Ti_3C_2T_x$ sheets (HF-HCl etching). Reproduced with permission from ref. [78]. Copy right from 2020 American Chemical Society.

position following –F desorption. The site redistribution or desorption of –F (Fig. 4d) or =O (Fig. 4e) in C 1*s* XPS show no change, resulting that the C atom was not directly involved in terminating species bonding. As a result, the persistent C 1*s* orbital rules out the bridge sites or hexagonal close-packed (HCP) sites between Ti and C atoms, i.e., the hollow sites of three Ti atoms above C atoms, as an alternative =O sites (Fig. 4f and g). Furthermore, Persson et al. [52] found no evidence that –OH was a terminating species. For MXenes terminated by =O, its vacancy lacks electrons, while the MXene terminated by –F has one extra electron vacancy than =O-terminated MXene; therefore, the orbit can be filled, and the structure stabilizes [87].

Li et al. [26] observed that molten salt etched MXene lacks –OH termination and MS-$Ti_3C_2T_x$ sample has =O-terminated surface functional groups, as shown by the fitting of the Ti 2*p* (Fig. 5a), O 1*s* (Fig. 5b), and C 1*s* (Fig. 5c) spectra. The existence of Ti–Cl bonds is confirmed by the XPS signal of the Cl 2*p* energy level (Fig. 5d). Elemental analysis found that the MS-$Ti_3C_2T_x$ MXene has an O-termination- specie content of about 12 wt% and a Cl termination-specie content of about 14 wt%, giving it a composition of $Ti_3C_{1.94}Cl_{0.77}O_{1.71}$. Xie et al. [3] presented DFT calculations showing reduced adsorption energy of Li onto =O-terminated MXenes compared to –OH-terminated MXene surfaces, resulting in greater interaction between O and Li and enhanced Li capacity. As a consequence, the high oxygen concentration and lack of OH surface groups of the MS-$Ti_3C_2T_x$ MXene in comparison to the particular molten salt fabrication technique are thought to contribute to the increased capacity. Peresson et al. [52] observed the effect of

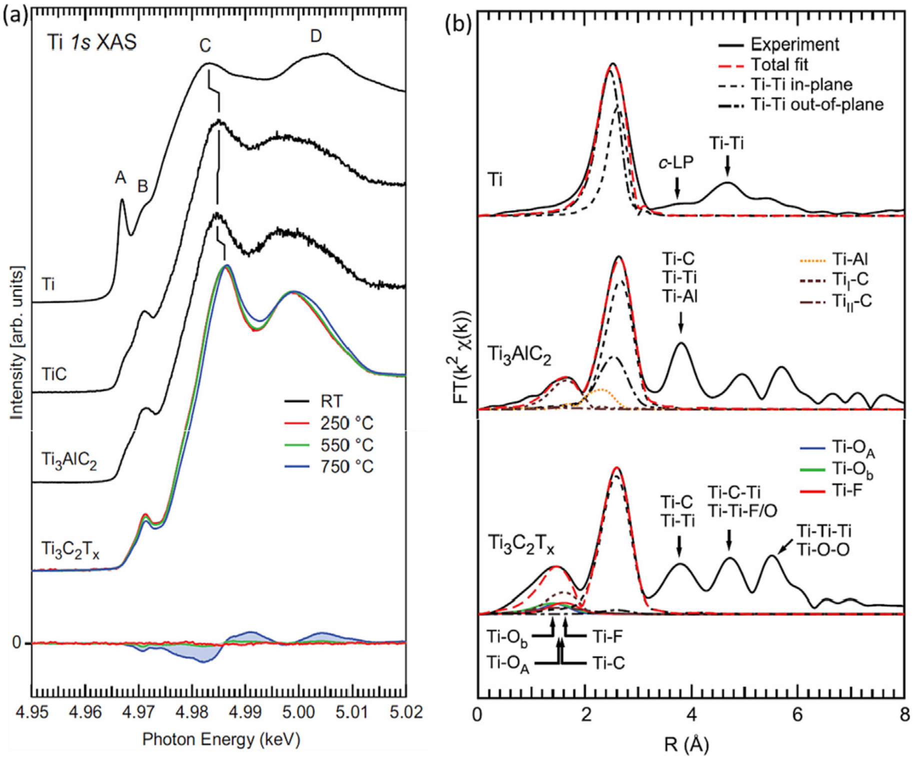

Fig. 3. (a) Ti 1*s* XANES spectra of Ti metal foil, TiC, Ti_3AlC_2, and $Ti_3C_2T_x$. After heat treatment at 250, 550, and 750 °C for 20 min, $Ti_3C_2T_x$ spectra were recorded at room temperature (RT) and 250 °C. Note that the red spectrum of $Ti_3C_2T_x$ heat-treated at 250 °C covers the black spectrum of unheated $Ti_3C_2T_x$. The difference between the RT $Ti_3C_2T_x$ spectra and spectra obtained after heat treatment at 250, 550, and 750 °C is shown at the bottom. (b) Fourier transform was obtained from k^2-weighted EXAFS oscillation of Ti metal foil, Ti_3AlC_2, and $Ti_3C_2T_x$. Reproduced with permission from ref. [36]. Copyright 2020. Physical Review Research 2 publishing group.

temperature on the surface terminating groups of $Ti_3C_2T_x$ MXene. Temperature-programmed XPS revealed that the functional groups were -F and =O and occupied distinct sites on the $Ti_3C_2T_x$ surface. The =O functional coordinates to two sites, whereas the functional –F coordinates to a single site. When the temperature rises over 550 °C, function –F progressively desorbs until it completely vanishes at 750 °C. The =O surface atoms coordinated with the alternative location (likely bridge site) move to the preferred coordination site vacated by –F desorption. Throughout the heating process, the C 1*s* spectra remained steady, showing that no C loss occurred. The F 1*s* peak intensity, on the other hand, decreases to a very small fraction of its original intensity in the temperature range of 550–750 °C. As a result, at high temperatures, F-terminations desorb from $Ti_3C_2T_x$ surfaces. In the O 1*s* spectrum, the peak at 529.9 eV decreased dramatically, while the third peak at 531.3 eV rose significantly after heat treatment at 750 °C; the latter dominates in the O 1*s* spectrum. The intensity redistribution was favorable to the formation of the Ti $2p_{3/2}$ peak at 455.1 eV and the Ti $2p_{1/2}$ peak at 461.2 eV, as was parallel to the Ti 2*p* peak. However, the Ti $2p_{3/2}$ and O 1*s* peaks were 455.1 and 531.3 eV, suggesting that the O-containing species can only be =O or –OH at 750 °C, after most –F desorption. Furthermore, during heat treatment, if both =O and –OH exist as surface terminating groups, one of them must be desorbed or changed to the other. However, there is no decrease in the integral intensity of the O 1*s* XPS peak indicates that –OH dissociation has not occurred because in this case, the dissociation product H will react with the adjacent –OH and synthesize H_2O, which will be desorbed immediately at elevated temperature (>500 °C), reducing the integral intensity of the O 1*s* spectrum; therefore, a considerable transformation from –OH to =O may be excluded. Furthermore, the conversion from =O to –OH necessitates a substantial quantity of hydrogen supply to the $Ti_3C_2T_x$ surface, which may be neglected. As a consequence, only one prediction remains: oxygen-containing species introduced during the etching process will persist during the heat treatment up to 750 °C [88]. Furthermore, it is difficult to move –OH terminating species at higher temperatures on the MXene surface; therefore, it is expected that the O 1*s* integral intensity will decrease and the O 1*s* signal should not show peak movement in XPS. In summary, the results of the TP-XPS investigation reveal that the =O terminating species are the only oxygen-containing terminating species that are mobile on the $Ti_3C_2T_x$ surface, occupying two adsorption sites on the $Ti_3C_2T_x$ surface that are stable at temperatures up to 750 °C.

3.5. TGA-MS study

Transition metal nitrides and carbides are thermally stable compounds in the bulk state with melting points from 2000 to 3000 °C [89]. It is critical to analyze decomposition properties and the thermal stability of 2D MXenes and their surface terminating groups [90,91]. The key to a variety of potential applications is regulating physicochemical parameters through surface functional groups modification [92–95]. Previous theoretical studies anticipated the terminal induced behavior from metallic to semiconductor in Ti_2CO_2 [96] as well as surface chemistry-dependent conductive and magnetic properties [20]. MXenes' thermal stability provides an upper limit for fabrication without structural deterioration, which is critical for metal matrix composites and ceramic [97]. With in-situ EELS and ex-situ thermogravimetric analysis using mass spectroscopy, Hart et al. [98] detected surface de-functionalization (TGA-MS) and de-intercalation. Vacuum annealing at higher temperatures after de-intercalation resulted in better electronic conductivity surface and de-functionalization. According to DFT calculations, the first species to desorb should be –OH [19,99], however, TGA-MS results showed loss of –OH at 375 °C for several samples as shown

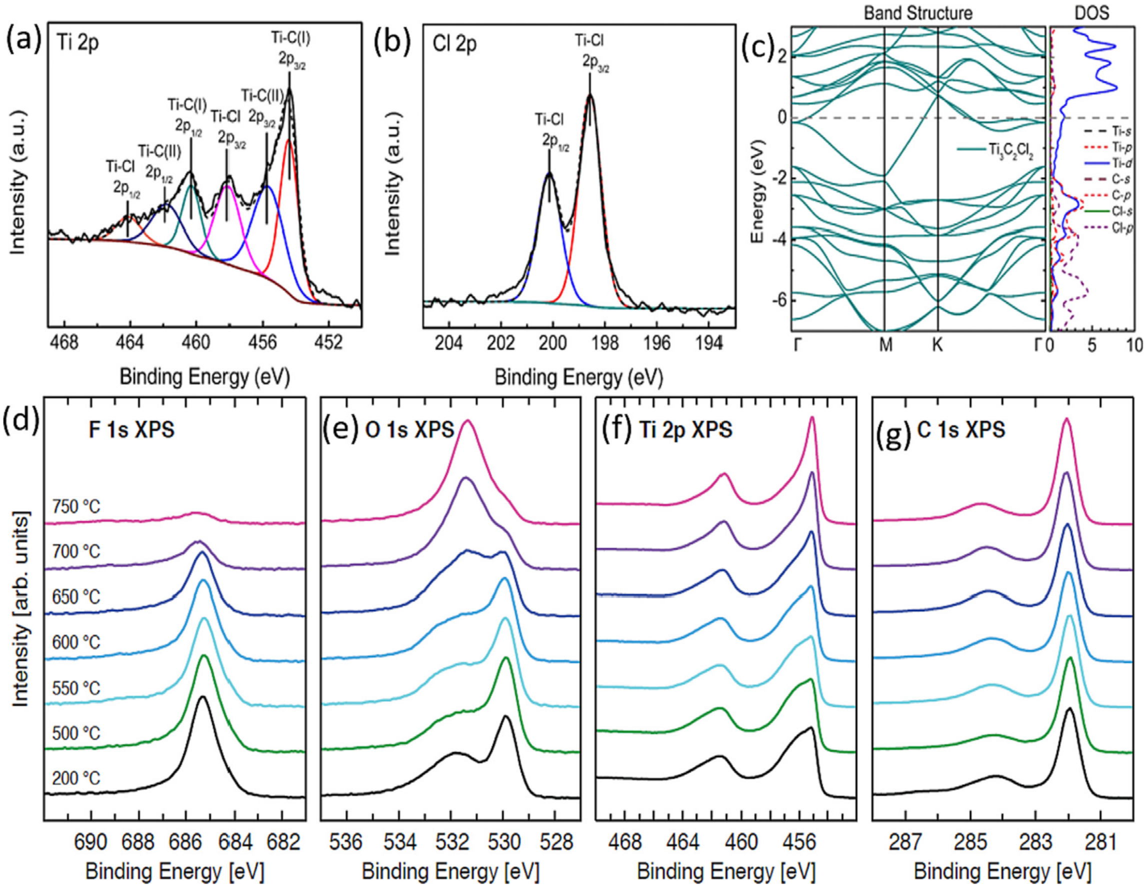

Fig. 4. (a) Ti 2*p* XPS spectrum of the as reacted product. (b) Cl 2*p* XPS analysis and (c) energy band structure of $Ti_3C_2Cl_2$. Reproduced with permission from ref. [22]. Copyright 2019. ACS publishing group. XPS spectra for the core energy levels (d) F 1*s*, (e) O 1*s*, (f) Ti 2*p*, and (g) C 1*s* of $Ti_3C_2T_x$. The spectra of the $Ti_3C_2T_x$ heated to 200 and 500 °C show only a difference in O 1*s* XPS, showing that O is redistributed between different positions. In steps of 50 °C between 500 and 750 °C, all spectra changed significantly except C 1*s* in the step of 50 °C, where the photon energy was 1486.6 eV. Reproduced with permission from ref. [86]. Copyright 2021. 2D Material (IOP) publishing group.

in Fig. 6(a). The release of de-protonated H_2O, on the other hand, entirely obscured the signal of –OH loss in the majority of TGA-MS data. Similarly, it is difficult to detect de-functionalization of –OH using in-situ EELS, possibly because the electron beam converts –OH groups into a stable terminating group (=O) before EELS acquisition [3]. On the other hand, the partially lost =O and –F species were easily identifiable. These species' release shows the loss of less stable –OH groups [19,40]. $Ti_3C_2T_x$ was annealed from 300 to 775 °C, resulting in a considerable loss of –F termination species and enhanced sample conductivity. After annealing at 500, 700, and 775 °C, in situ EELS measurements indicate a reduction in the F *K*-edge intensity, indicating partial de-functionalization of the –F functional group. Ex-situ TGA-MS data demonstrate the release of –F termination starting approximately 400 °C, which is consistent with the EELS results (Fig. 6b). At 150 °C, the wide peak in the m/e = 19 ion channel strongly matches the H_2O channel, which shows that this peak is caused by a process similar to H_2O de-intercalation, such as protonated H_2O release. Peak 1 in the O *K*-edge EELS spectra is consistent with Persson et al. [52] observations as shown in Fig. 6 (c), suggesting that there is no indication for the loss of =O terminating groups, although there was a considerable loss of –F. Persson et al. [52] observe that in-situ annealing of $Ti_3C_2T_x$ using scanning TEM (STEM) and XPS investigation, where they show loss of –F commencing at 400 °C and preservation of =O terminations. Sang et al. [41], on the other hand, stated that electron irradiation and over 500 °C annealing, the huge voids that occurred on the removal of =O terminations which might be attributable to beam-induced effects.

Furthermore, using low-dose DD EELS [100] enables faster collection times, lowering the risk of beam-induced sample deterioration even further (Fig. 6d–f) [98]. From a detailed analysis of in-situ heating and biasing experiments, Hart et al. [98] identified changes from semiconductor to metallic behavior in $Mo_2TiC_2T_x$ and Ti_3CNT_x after the annealing-induced loss of intercalated species based on extensive investigation of biasing experiments and in-situ heating. These transitions illustrate that $Mo_2TiC_2T_x$ and Ti_3CNT_x intra-flake metallicity shows how intercalants in multi-layer MXenes can produce negative d*R*/d*T*. Second, the conductivity of all three MXenes was enhanced by high-temperature annealing and the partial loss of surface terminations (Fig. 6d–f, bottom insets). This observation supports previous assumptions that non-terminated MXenes with high carrier concentrations show metallic behavior [24,42,101,102]. As a function of annealing temperature, there is a link between changes in $Ti_3C_2T_x$–F concentration and RT resistance. The loss of –OH group is likely a substantial contributor to the decrease in sample resistance during annealing phase at 500 °C. A minor contribution from the last steps of H_2O deintercalation may also be observed. Ex-situ TGA-MS (Fig. 6b) and in situ EELS (Fig. 6c) demonstrate no indication of additional H_2O loss following the 500 °C annealing stage.

Furthermore, XRD measurements have demonstrated that annealing above 500 °C does not affect the $Ti_3C_2T_x$ c-lattice spacing [103]. The improvement in $Ti_3C_2T_x$ conductivity during annealing stages at 700 and 775 °C is solely related to the loss of –F terminations since there is no change in inter-flake spacing, no observation of a conducting secondary phase, and no

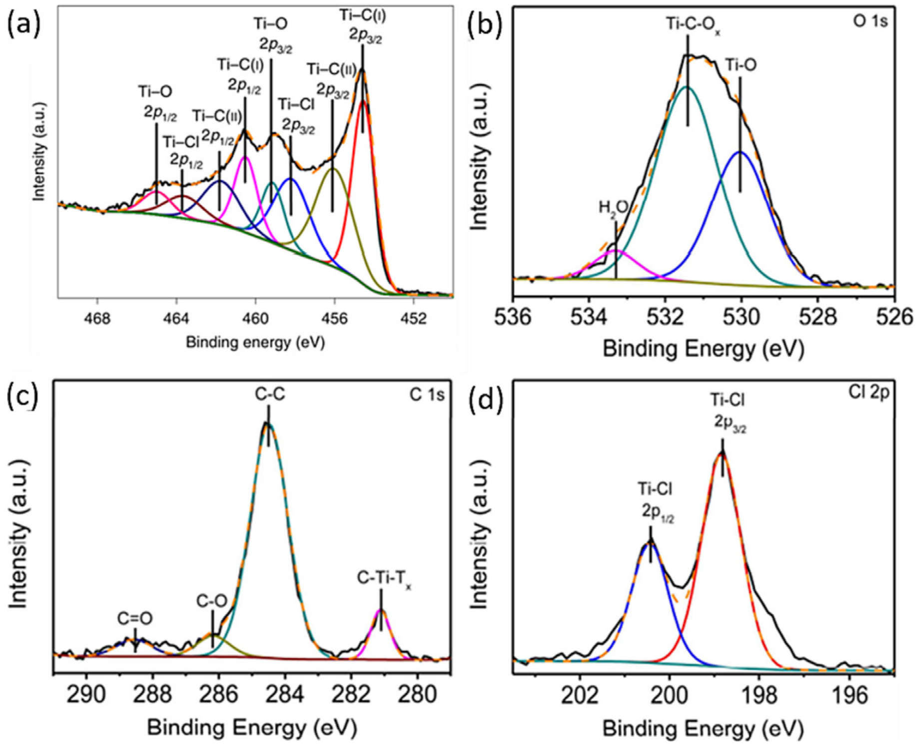

Fig. 5. Structural and morphological characterizations of molten salt MXene (MS-$Ti_3C_2T_x$). (a) XPS analysis of the Ti 2*p* energy level, (b) O 1*s* (c), C 1*s*, and (d) Cl 2*p* energy level from the MS-$Ti_3C_2T_x$ MXene sample. Reproduced with permission from ref. [26]. Copyright 2020 Nature Materials.

indication of intercalation loss [104]. In situ annealing of Ti_3CNT_x at 500 and 700 °C eliminate the –F species and enhanced conductivity, similar to $Ti_3C_2T_x$ [98]. A Ti_3CNT_x sample was measured using time-resolved in situ EELS in addition to the Ti_3CNT_x sample reported before in the text and given in Fig. 6 (d–f). These results reveal that the loss of terminal species has an impact on the electrical characteristics of MXene. Surface de-functionalization for $Mo_2TiC_2T_x$ was observed at lower temperatures than for Ti_3CNT_x or $Ti_3C_2T_x$, implying a comparatively weaker interaction between Mo atoms and surface terminating groups than Ti atoms [98]. In situ EELS reveals that annealing $Mo_2TiC_2T_x$ at 700 and 775 °C results in a significant decrease in the =O concentration, whereas annealing at 500 °C results in the total loss of –F. The resistivity of $Mo_2TiC_2T_x$ dropped by 32% as =O terminations were largely removed from the surface. These results suggest that the elimination of =O terminating group from $Mo_2TiC_2O_x$ enhances the intra-flake conductivity of MXene [105,106].

4. Stability of MXene surface terminators on transition metal (M)

It is difficult to precisely manage terminations or disclose their influence due to the intricacy of terminations with different compositions and varied species. On the other hand, First-principles computations provide a reliable way to immediately determine the structural and performance implications of terminations. The chemical and physical characteristics of MXenes, including optical [107], magnetic [20], thermoelectric [108], electronic [109,110], and mechanical [85] features, have been studied using first-principles simulations. Prior to the modeling of MXene structures, bonding characteristics between surface terminations and transition metals are identified. $Mo_2TiC_2T_x$ had a higher degree of surface de-functionalization than Ti-based MXenes, and –F terminations were less stable than oxygen terminations. These findings provide a way to boost MXene applications' performance even further. Mono-M $M_4X_3T_x$ and $M_3X_2T_x$ have metallic conductivity in general, however some out-of-plane ordered double transition metal (DTM) MXenes can be semi-metals or semiconductors [111,112]. Surface de-functionalization for $Mo_2TiC_2T_x$ happened at lower temperatures than for Ti_3CNT_x or $Ti_3C_2T_x$, implying a weaker interaction between surface Mo atoms and termination species than for Ti atoms. After annealing at 500 °C, in situ EELS revealed the total loss of –F from $Mo_2TiC_2T_x$, and annealing at 700 and 775 °C resulted in a significant decrease in the =O concentration (Fig. 7a). The $Mo_2TiC_2T_x$ resistance dropped by 32% when the =O terminations were largely removed from the surface (Fig. 7b). These results propose that the release of =O from $Mo_2TiC_2O_x$ improves the MXene intra-flake conductivity [105,106].

It's worth noticing that MXene conductivity varies depending on the precursors and synthesis procedure. The electrical conductivity of $Nb_yV_{2y}CT_x$ and $Ti_yNb_{2y}CT_x$ films diminishes with increasing Nb concentration in the solid solution MXenes. This means that MXenes' electrical conductivity may be changed by changing their chemical composition [113].

5. Relation between conductivity and terminating groups of MXene

Surface terminations, which are added during MXene synthesis [81], are thought to govern metal-to-insulator transitions [106,111], as well as alter functional characteristics including Li-ion capacity [24], band alignment [114], magnetism [115], superconductivity [116], and mechanical properties [96]. In situ annealing of Ti_3CNT_x at 500 and 700 °C reduced –F species and enhanced electrical conductivity, similar to $Ti_3C_2T_x$. The simultaneous release of –F termination species and a rise in electronic conductivity are seen in time-resolved studies of Ti_3CNT_x (Fig. 8a and b). This data also shows that the loss of terminal species has an impact on the electrical characteristics of MXene. To understand the as-

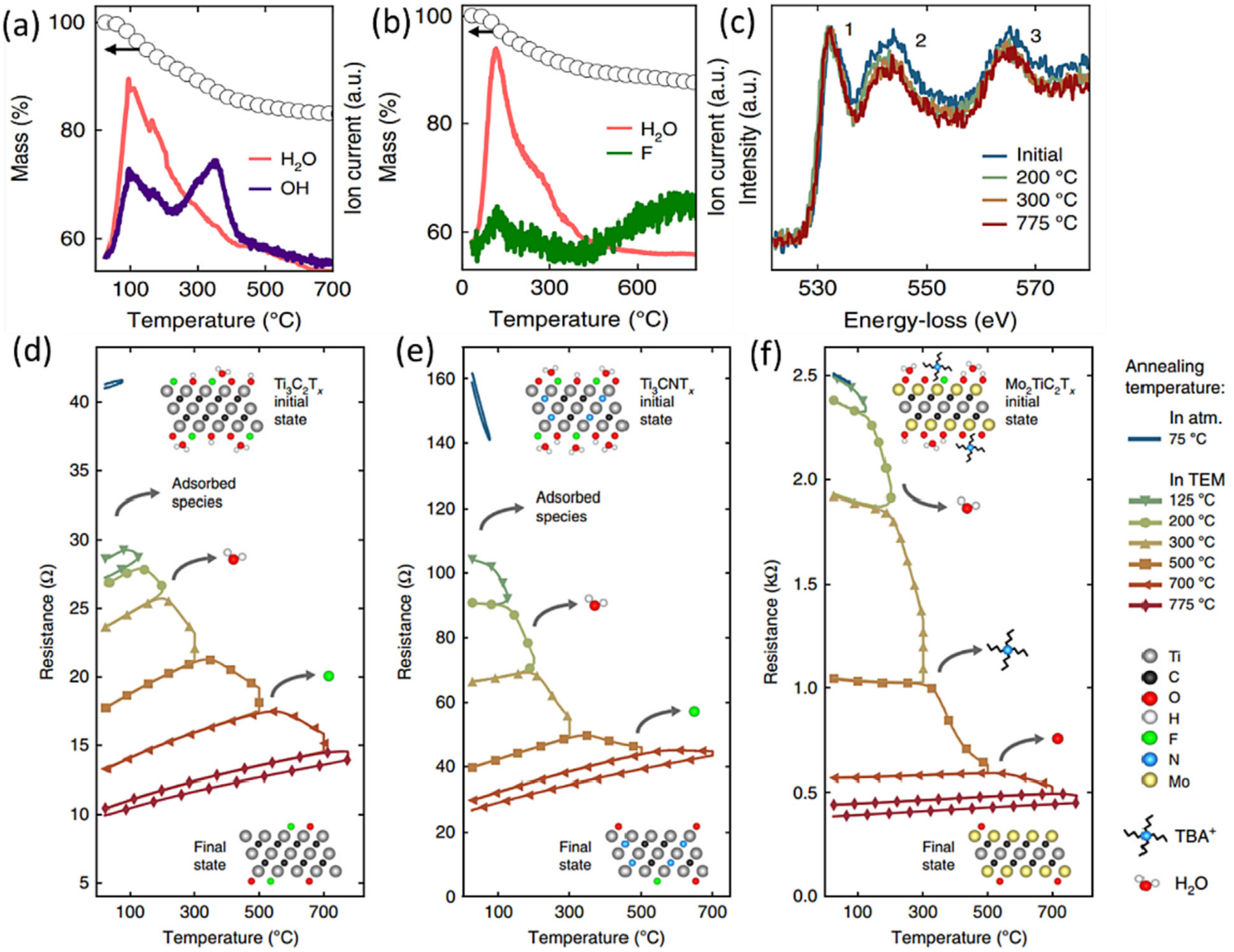

Fig. 6. TGA-MS of Ti_3CNT_x illustrates the loss of –OH terminating group and H_2O intercalants (a). The loss of H_2O intercalants during annealing is indicated by in situ EELS of the standardized O *K*-edge of Ti_3CNT_x (b). TGA-MS of $Ti_3C_2T_x$ reveals that the de-intercalation of H2O is completed by 400 °C, while the –F de-functionalization begins at 400 °C (c). The retention of ═O and the loss of intercalated H_2O of $Ti_3C_2T_x$ O Kedge's in-situ EELS after annealing can be seen from the substantial decline in peaks 2 and 3 compared to peak 1. For $Ti_3C_2T_x$ (d), Ti_3CNT_x (e), and $Mo_2TiC_2T_x$ (f), the evolution of MXene electronic characteristics is demonstrated using in situ vacuum annealing. Various vacuum annealing processes in the TEM were used to accomplish the experiments. Each phase of the vacuum annealing process has its own symbol and color. The cooling and heating curves are displayed for each annealing stage. The resistance decreased during annealing in all cases, hence the cooling curve always falls below the heating curve. Insets depict the atomic structures of several MXenes. Ti_3CNT_x and $Ti_3C_2T_x$ have intercalated water molecules on their surfaces in the initial state schematics, whereas $Mo_2TiC_2T_x$ has TBA^+ and water molecules on its surface. The loss of terminating species, intercalants, and adsorbed species during annealing has an impact on MXene sample resistance. Reproduced with permission from ref. [98]. Copyright 2019 Nature communications.

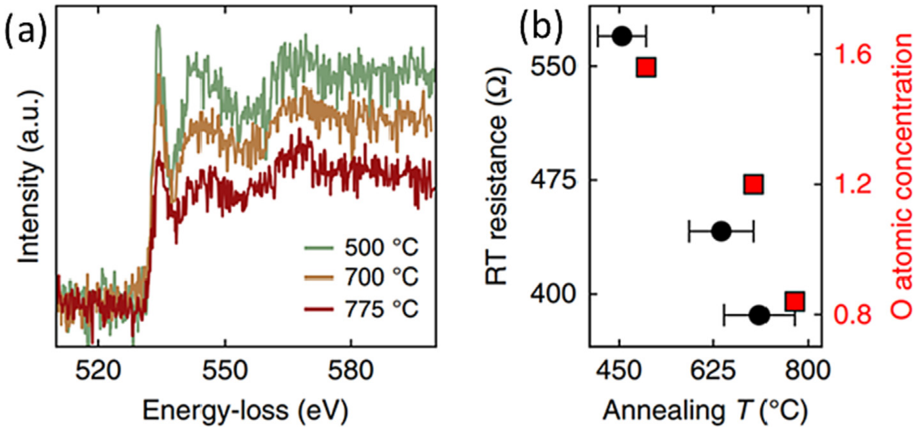

Fig. 7. (a) In-situ EELS spectra of the O *K*-edge of $Mo_2TiC_2T_x$. (b) comparison of the concentration of ═O (represented as red squares) with the post-anneal RT resistance (represented as black circles), both expressed in units of *x* based on the chemical formula $Mo_2TiC_2O_x$. Reproduced with permission from ref. [98]. Copyright 2019 Nature Communications.

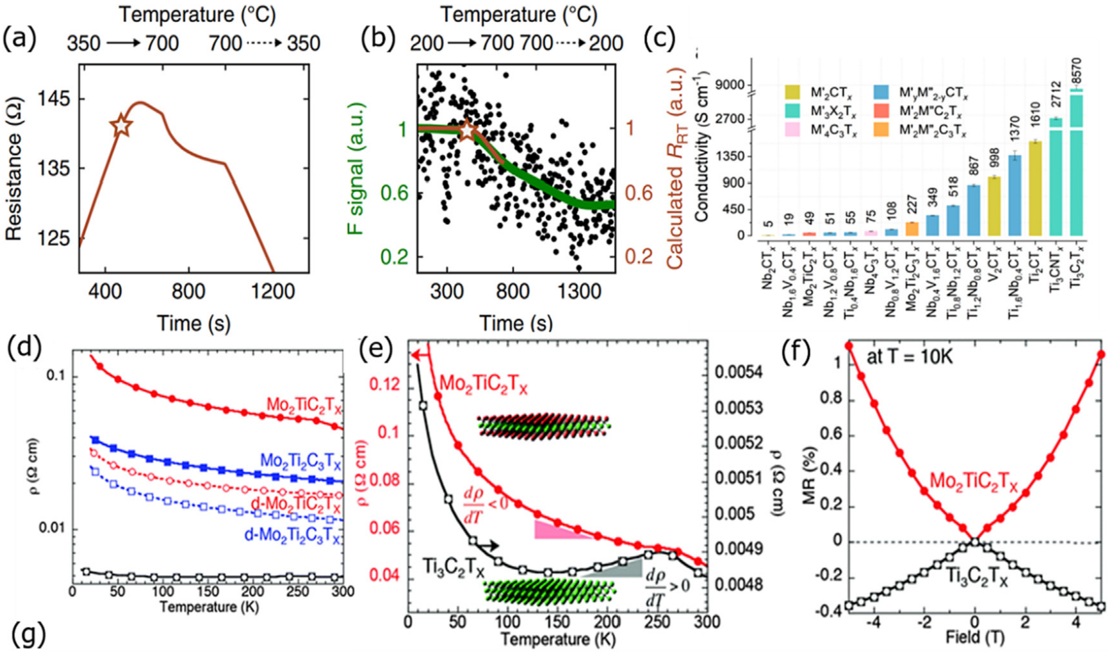

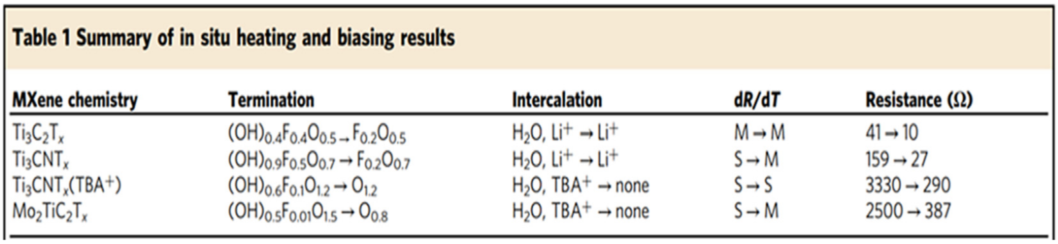

Table 1 Summary of in situ heating and biasing results

MXene chemistry	Termination	Intercalation	dR/dT	Resistance (Ω)
$Ti_3C_2T_x$	$(OH)_{0.4}F_{0.4}O_{0.5} \rightarrow F_{0.2}O_{0.5}$	H_2O, $Li^+ \rightarrow Li^+$	M → M	41 → 10
Ti_3CNT_x	$(OH)_{0.9}F_{0.5}O_{0.7} \rightarrow F_{0.2}O_{0.7}$	H_2O, $Li^+ \rightarrow Li^+$	S → M	159 → 27
$Ti_3CNT_x(TBA^+)$	$(OH)_{0.6}F_{0.1}O_{1.2} \rightarrow O_{1.2}$	H_2O, $TBA^+ \rightarrow$ none	S → S	3330 → 290
$Mo_2TiC_2T_x$	$(OH)_{0.5}F_{0.01}O_{1.5} \rightarrow O_{0.8}$	H_2O, $TBA^+ \rightarrow$ none	S → M	2500 → 387

Fig. 8. The time-resolved resistance (a) and F *K*-edge intensity of Ti_3CNT_x during in situ annealing (b). Heating is represented by the solid (dashed) arrows. *t* = 0 s refers to the start of annealing at RT on the time axis. The stars denote the highest temperature of the previous annealing, which was 500 °C. The EELS data is smoothed with a Gaussian smooth in (b) (black circles). The estimated RT resistance in (b) is represented by the dark orange line, which was derived using the observed value of dR/dT during heating. This calculation is only applicable up to 700 °C since dR/dT varies with annealing. Both calculated RT resistance and the -F concentration were adjusted by their initial values to normalized it. Reproduce with permission from ref. [98] Copyright from Nature Communications 2019. (c) The electrical conductivity of different vacuum filtered MXene films. Reproduce with permission from ref. [119]. Copyright 2020, American Chemical Society. (d) The resistivity of $Ti_3C_2T_x$ (black), $Mo_2TiC_2T_x$ (blue), and $Mo_2TiC_2T_x$ (red) as a function of temperature. Multilayered powders are represented by solid lines while delaminated films are represented by dashed lines. (e) Resistivity findings of $Ti_3C_2T_x$ (black, right-side y-axis) and $Mo_2TiC_2T_x$ (left, red side y-axis). The d*R*/d*T* discrepancies are shown by the colored triangles (black and red) underneath each resistivity curve. (f) Comparison of $Mo_2TiC_2T_x$ (red, left side *y*-axis) and $Ti_3C_2T_x$ (black, right-side *y*-axis) resistivity results. Reproduce with permission from ref. [106]. Copyright from RSC. (g) For $Ti_3C_2T_x$, Ti_3CNT_x, Ti_3CNT_x (TBA^+), and $Mo_2TiC_2T_x$ represent changes induced during in-situ vacuum annealing up to 775, 750, 700, and 775 °C, respectively. S indicates semiconductor-like conduction (negative d*R*/d*T*) and M shows metallic conduction (positive d*R*/d*T*) in the d*R*/d*T* column. In-situ EELS was used to determine the reduction in =O and –F terminating groups whereas ex-situ TGA-MS was used to detect –OH terminations and the loss of intercalants. Reproduce with permission from ref. [98]. Copyright from Nature communications 2019.

prepared sample characteristics, Hart et al. [98] investigated the temperature-dependent resistance of samples that were originally evaluated in the ambient environment from room temperature (RT) to 75 °C. $Mo_2TiC_2T_x$ and Ti_3CNT_x exhibited semiconductor-like (negative d*R*/d*T*) behavior whereas $Ti_3C_2T_x$ exhibited metallic behavior, as found in earlier literature (Fig. 8g) [117,118]. To further understand the relationship between the electrical conductivity of MXene films, the four-point probe method was used to measure the electrical conductivity of all vacuum-filtered MXene films. Ti-based MXenes (Ti_2CT_x, Ti_3CNT_x, $Ti_{1.6}Nb_{0.4}CT_x$, and $Ti_3C_2T_x$), as well as V_2CT_x, have electrical conductivities more than 1000 S cm^{-1}, but Nb-based MXenes have comparatively low electrical conductivities, as illustrated in Fig. 8(c) [113]. It is worth noting that MXene conductivity varies depending on the precursors and synthesis procedure. The electrical conductivity of $Nb_yV_{2y}CT_x$ and $Ti_yNb_{2y}CT_x$ flakes diminishes with increasing Nb concentration in the solid solution MXenes.

This means that MXenes' electrical conductivity can be adjusted by changing their chemical composition. $Mo_2TiC_2T_x$ exhibits semiconductor-like behavior, but it's unclear whether this is due to extrinsic (intercalation, inter-flake hopping) or intrinsic ($M_{n+1}X_nT_x$ stoichiometry) effects [106]. The resistivity values of a multilayered $Mo_2TiC_2T_x$ (red, left-hand y-axis) and a multilayered $Ti_3C_2T_x$ (black, right-hand *y*-axis) are displayed in Fig. 8(e) to better highlight the difference between $Mo_2TiC_2T_x$ and $Ti_3C_2T_x$ MXenes. Both samples indicate a shift in behavior towards 250 K, which is likely due to ions and water present between the MXene layers. In contrast to $Mo_2TiC_2T_x$, which has a resistivity that rises with decreasing temperature (d*ρ*/d*T*< 0) from 10–250 K, $Ti_3C_2T_x$ has a metallic behavior from 130 to 250 K (d*ρ*/d*T*> 0). The resistivity of $Ti_3C_2T_x$ rises with decreasing temperature at temperatures below 130 K [106]. An Arrhenius model explaining basic semiconductor behavior or any variable range hopping model cannot effectively suit the $Mo_2TiC_2T_x$ data given in Fig. 8(d). Alternatively, there might be alternative reasons for the slight improvements in resistivities with lowering temperatures seen in Fig. 8(d and e), such as interflake hopping mechanisms. A clear research direction is required before comes to any conclusion. Regardless of this remark, it is obvious that when Mo layers sandwich their Ti atomic layers (in Mo-based MXenes), resistance grows monotonically with decreasing temperature, but when Mo is absent, initially resistance decreases with decreasing temperature, at least initially as given in Fig. 8(e and f) [106].

6. Byproducts of oxidized MXene

2D material MXenes has a large family that is being studied extensively for a wide variety of uses, is unstable in water, producing TiO_2 spontaneously. Based on solution pH measurements and solid product characterization, many ideas have recently been offered to explain MXene conversions in aqueous conditions. MXene reactivity is obviously significant for storage, device manufacturing, synthesis, and various other applications. MXenes are often stored, processed, and synthesized using water colloids, which are also employed in various device assembling. As a result, MXenes' chemical interaction with water is crucial. It's plausible to assume that nitrogen and carbon will eventually convert into gaseous species, such as N_2, CO_2, CH_4 so on, as a consequence of these transformations [120]. The reaction of group IV metal carbides with water, which produces hydroxides and hydrocarbons, was first described by Avgustinik et al. [121] a long time ago. According to the previous literature, the carbide carbon stays in the form of "carbon" after MXene decomposition [54,90,122,123]. Huang et al. [124] stated that the transformations of metal carbonatite and carbide structures in water convert into CH_4. The evolved gases of MXene were analyzed using a GC apparatus with a thermal conductivity detector (Fig. 9a), which is not especially sensitive to CO_2. Fig. 9(b) shows the Raman spectra of gas-phase bubbles evolved in sealed glass vials and collected. The symmetric stretching mode of N_2 is represented by the peak at 2331 cm^{-1}, which is likely due to the little quantity of air dissolved in DI water [125], whereas the asymmetric and symmetric CH stretching modes in methane are represented by the peaks at 3020 and 2918 cm^{-1}, respectively [126]. The rotating Raman spectrum of CH_4 is represented by the surrounding sequence of regularly spaced smaller peaks in the 2850–3200 cm^{-1} region. As a result, Raman spectroscopy supports GC data of CH_4 synthesis during carbonitride and carbide MXene conversions in water. Despite the fact that these gaseous products would be predicted in an oxidative breakdown of MXenes, no traces of CO or CO_2 were detected in Raman or GC, contrary to previously reported hypotheses [120,127].

In an aqueous environment, the transformation rates of MXenes with common transition metals are dependent on monolayer thickness and are lower for pure carbide MXenes than carbonitride MXene. When the monolayer structure and thickness are the same, but different transition metals (for example, Nb_2CT_x and Ti_2CT_x) can have enormously different chemical reactivities, representing that the chemical properties of MXene are also dependent on the type of bonding within the monolayer and their chemical composition. The impacts of different MXene flake sizes are less substantial in this context when compared to the effects of composition and monolayer thickness [124].

7. Conclusions and future prospective

Despite the inspiring progress that has been made, there are still a number of critical issues of MXenes that need to be resolved before their practical applications. As a result of the exfoliation process, MXenes' surface properties are highly reliant on the different kinds and concentrations of surface terminators. In addition, new synthetic methods must be developed to ensure uniform surface terminations and high quality bare MXenes in the preparation. The regulation of MXenes has evolved into an active research area as more and more methods for achieving MXenes have been discovered. Based on current findings, we believe that the following are important researches aspects for MXene terminations.

1. UPS/XPS analyses reveal that in $Ti_3C_2T_x$, –OH is not an essentially produced terminating group, which is unexpected but not inconsistent with prior studies [86]. The previous XPS study only proposed that the broad characteristic peak at 531.8 eV in the O 1*s* XPS spectrum included –OH species, [52] even though it was not caused by the spectral shape. The joint temperature-programmed XPS/STEM study shows that the wide characteristic peak at 531.8 eV in the O 1*s* XPS spectrum originates from the =O terminating group at the fcc site [128]. In addition, $Ti_3C_2T_x$ nanosheets are very prone to oxidize, and the oxidized section is just a few Ångström thick; therefore, –OH will remain quite close to C. As a result, the use of –OH as the intrinsic termination species in $Ti_3C_2T_x$ is based only on assumption. The

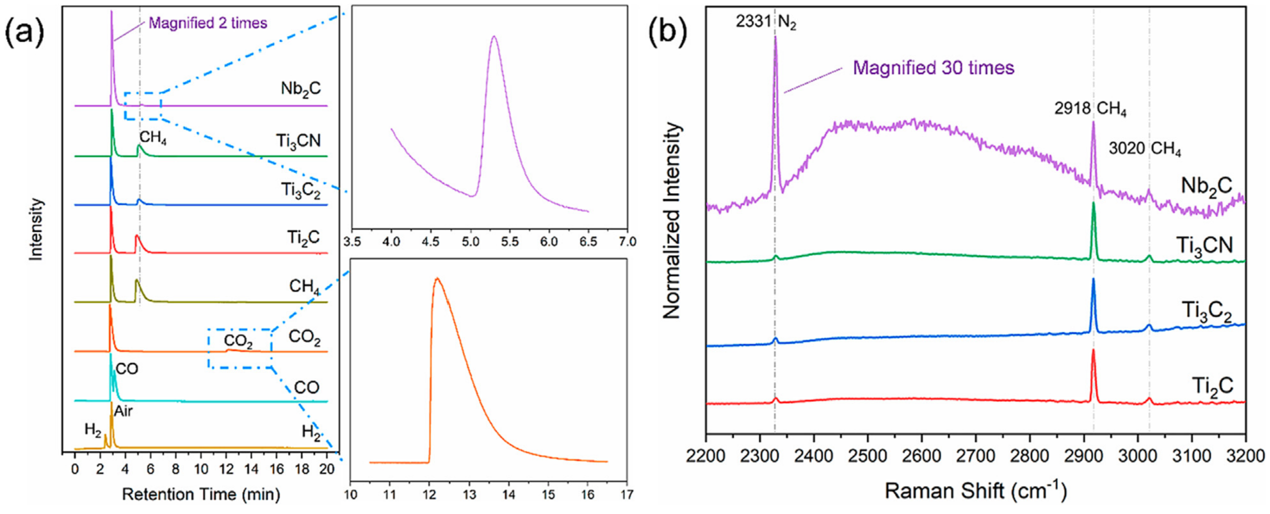

Fig. 9. (a) Gaseous products like H_2, CO, CO_2, and CH_4 evolved from $Ti_3C_2T_x$, Ti_2CT_x, Nb_2CT_x, and Ti_3CNT_x MXenes in water were analyzed using gas chromatography (GC). The right-hand insets show a magnified region of the CH_4 peak formed by the CO_2 peak of reference CO_2 and Nb_2CT_x MXene degradation. (b) Raman spectra of gas bubbles in sealed vials were examined and collected for $Ti_3C_2T_x$, Ti_2CT_x, Nb_2CT_x, and Ti_3CNT_x MXene conversions in water. Reproduced with permission from ref. [124]. Copyright ACS nano 2020.

results reveal that Ti 3*p* – F 2*p* hybridization dominates the chemical connection between the $Ti_3C_2T_x$ surface and fcc site –F. On the other hand, the chemical bond between the $Ti_3C_2T_x$ surface and fcc =O is primarily controlled by Ti 3*p*

2. =O 2*p* hybridization, with considerable contributions from the Ti 3*d* and Ti 4*p* states. These findings are important for predicting the intercalation process of future energy storage devices because they provide critical information for understanding the specific properties of MXenes.
3. It is also observed that –OH and –F terminating groups, as well as H_2O, were still present in the ^1H and ^{19}F NMR spectra of $Ti_3C_2T_x$ MXene after vacuum drying at 200 °C. The connectedness of the –OH and –F terminations was validated by two-dimensional correlation studies, which demonstrated that they both occurred in extremely close proximity between 2D metal carbide layers. Quantitative NMR measurements demonstrate that –OH termination is substantially lower than –F and =O termination, and surface termination is strongly dependent on the synthesis method utilized; for example, the -F termination of HF composites is nearly-four times that of LiF-HCl composites. If the synthesized sample evaporated overnight drying at 60 °C, then there must be a very low peak for –OH termination in the NMR spectra and When the MAX phase is etched with alkali, the –F termination vanishes completely, leaving just the –OH and =O terminators [35]. Etching in polar organic solvents can be utilized to enhance the –F termination ratio while decreasing the –OH termination ratio [129]. Several efforts to modify the MXene sheet surface terminating species after etching was also observed. These approaches, on the other hand, rely on high-energy treatments (such as high-temperature annealing), which leads to structural degradation of the MXene [98].
4. =O-terminated MXenes have a greater energy storage capacity than –OH-terminated MXenes; therefore, it is critical to use =O-terminated MXenes for energy storage. By using anhydrous HCl and LiF solution, =O-terminated MXene can be synthesized.
5. Many theoretical investigations have discovered that in the process of tailoring attributes, substituting the inherently produced termination species with alternative terminating species is not a problem. However, there is no conclusive experimental evidence that naturally occurring terminating species may be substituted (re-terminated) [87].
6. The fitting of XPS for the characterization of $Ti_3C_2T_x$ is a serious issue that makes fitting more perplexing. Certain materials may get energy during XPS analysis because the spectra tend to shift toward higher BE values. The spectrum must be calibrated to resolve this issue. The fact that this approach relies on carbon impurities is one of its drawbacks. Several reports utilize any figure between 284.5 and 285.0 eV, making it impossible to calibrate accurately. Because of the 0.5 eV discrepancy, proper calibration is not possible [130]. The second method is to use the renowned BEs by adding noble metal powder (such as Au or Ag) to the sample [131]. This approach is not addressed and has never been utilized in the MXene literature.
7. New synthetic strategies are widely preferred to control surface termination of MXene. Advanced characterization technologies, especially operando methods, are crucial. Surface terminations can be used to tailor MXenes' electrochemical performance. Various calculated results shows that ion diffusion and adsorption processes are profoundly affected by surface terminators of MXenes that interact with ions directly. Post-processing, such as alkali treatment and annealing, influences the terminating groups and required future attention. As an example, the –F and –OH terminations of MXenes in ion batteries have been shown to reduce their capacity [24]. The capacity of MXenes can be significantly increased by optimizing the ratio of =O, –F and –OH terminations [25]. Theoretical capacities of Ti_3C_2, $Ti_3C(OH)_2$, $Ti_3C_2F_2$, and $Ti_3C_2O_2$ MXenes are 320, 76, 130, and 268 mAh g^{-1}, respectively for Li-ion batteries [3,24,25]. The surface terminations of MXenes can be effectively modified by heteroatom doping and heat treatment, resulting in significant improvements in MXene performance in energy storage devices. It is also observed that large atomic radius of non-halogen elements was better for energy storage led researchers to arrange different possible terminations on the surface of MXenes, such as –S and N. Additionally, phonon frequency analyses show that other terminations like –N and –S are also theoretically stable, this opens the door to further tinkering with MXenes. =O-terminated MXenes have higher mechanical properties and smaller lattice parameters than –OH and –F terminations. Interlayer spacing is also dependent on the atomic size of surface terminating groups. MXenes are predicted to perform better with =O, –S, and –N terminations than –OH and –F.
8. In HER, there are several ways to improve the stability of the MXene-based catalyst, including adding antioxidation agents and carbon as well as the optimization of preparation conditions. In spite of the fact that a few layers of MXenes have superior catalytic effects due to their larger surface area and, as a result, better electronic conductivity, however, multilayer MXenes have been shown to be more stable than those with only a few layers. Consequently, it remains essential to optimize the MXene layers and compositions to achieve a balance between catalytic activity and stability. Therefore, for actual operations, it is essential to investigate the long-term stability of the catalysts. The HER activity of MXenes may be enhanced by concurrently doping metal, etching two or more MAX, and etching MAX simultaneously. In the future, new MXenes with five or more transition metal atomic layers may have excellent HER performance based on the newly discovered MXenes i.e., $Mo_4VC_4T_x$ and $W_{1.33}CT_x$, $Mo_5C_4T_x$, $Mo_4TiC_4T_x$ MXenes. MXenes with some surface terminal groups (–Cl, –Br, –I, –S, –Te, –Po) synthesized by molten salt (Lewis' acid) etching may also give significantly better HER activity than those with –F, =O, –OH terminating groups, thus leading to the discovery of more new surface terminations. Novel MXenes materials produced from precursors other than the MAX phase may exhibit novel HER properties. New MXene nanostructures can be produced through minimizing the lateral size to the nanoscale, and the addition of 3D open porous networks or other high-HER active materials can further enhance the HER properties.

These insights open up new possibilities for MXene applications like catalysis, optoelectronics, energy storage and conversions, and electromagnetic interference shielding. Improved conductivity is required in other applications, such as catalysis, energy storage and, triboelectrics, where functionalized MXene surface chemistry provides chemical advantages. As a result, more research is required to learn how partial de-functionalization affects performance in these domains.

Declaration of competing interest

The authors declare that they have no known competing financial interests or personal relationships that could have appeared to influence the work reported in this paper.

Acknowledgments

This work was supported by the National Natural Science Foundation of China (21703147 and U1401248). One of the authors (T. B.) also acknowledges the support of China Scholarship Council (2018SLJ022487).

References

[1] M. Naguib, V.N. Mochalin, M.W. Barsoum, Y. Gogotsi, Adv. Mater. 26 (2014) 992–1005.
[2] M. Naguib, M. Kurtoglu, V. Presser, J. Lu, J. Niu, M. Heon, L. Hultman, Y. Gogotsi, M.W. Barsoum, Adv. Mater. 23 (2011) 4248–4253.
[3] Y. Xie, M. Naguib, V.N. Mochalin, M.W. Barsoum, Y. Gogotsi, X. Yu, K.-W. Nam, X.-Q. Yang, A.I. Kolesnikov, P.R. Kent, J. Am. Chem. Soc. 136 (2014) 6385–6394.
[4] O. Mashtalir, M. Naguib, V.N. Mochalin, Y. Dall'Agnese,, M. Heon, M.W. Barsoum, Y. Gogotsi, Nat. Commun. 4 (2013) 1–7.
[5] S. Yang, J. Yao, H. Hu, Y. Zeng, X. Huang, T. Liu, L. Bu, K. Tian, Y. Lin, X. Li J. Mater. Chem. A 8 (2020) 23498–23510.
[6] T. Bashir, X. Li, S. Yang, Y. Song, S. Zhou, J. Wang, W. Zhu, J. Yang, J. Zhao, L. Gao, J. Alloys Comp. (2022) 166213.
[7] X. Liang, A. Garsuch, L.F. Nazar, Angew. Chem. 127 (2015) 3979–3983.
[8] Z. Wang, K. Yu, S. Gong, E. Du, Z. Zhu, Nanoscale 12 (2020) 18950–18964.
[9] P. Ma, D. Fang, Y. Liu, Y. Shang, Y. Shi, H.Y. Yang, Adv. Sci. 8 (2021) 2003185.
[10] M.K. Aslam, T.S. AlGarni, M.S. Javed, S.S.A. Shah, S. Hussain, M. Xu, J. Energy Storage 37 (2021) 102478.
[11] S. Bai, M. Yang, J. Jiang, X. He, J. Zou, Z. Xiong, G. Liao, S. Liu, 2D Mater. Appl. 5 (2021) 1–15.
[12] X. Xie, N. Zhang, Adv. Funct. Mater. 30 (2020) 2002528.
[13] M.R. Lukatskaya, O. Mashtalir, C.E. Ren, Y. Dall'Agnese, P. Rozier, P.L. Taberna, M. Naguib, P. Simon, M.W. Barsoum, Y. Gogotsi, Science 341 (2013) 1502–1505.
[14] Q. Jiang, N. Kurra, M. Alhabeb, Y. Gogotsi, H.N. Alshareef, Adv. Energy Mater. 8 (2018) 1703043.
[15] S. Zhou, C.L. Chiang, J. Zhao, G. Cheng, T. Bashir, W. Yin, J. Yao, S. Yang, W. Li, J. Wang, Adv. Energy Mater. (2022) 2112592.
[16] H. Riazi, S.K. Nemani, M.C. Grady, B. Anasori, M. Soroush, J. Mater. Chem. A 9 (2021) 8051–8098.
[17] F. Liu, A. Zhou, J. Chen, J. Jia, W. Zhou, L. Wang, Q. Hu, App. Surface Sci. 416 (2017) 781–789.
[18] M. Naguib, O. Mashtalir, J. Carle, V. Presser, J. Lu, L. Hultman, Y. Gogotsi, M.W. Barsoum, ACS Nano 6 (2012) 1322–1331.
[19] M. Ashton, K. Mathew, R.G. Hennig, S.B. Sinnott, J. Phys. Chem. C 120 (2016) 3550–3556.
[20] M. Khazaei, M. Arai, T. Sasaki, C.Y. Chung, N.S. Venkataramanan, M. Estili, Y. Sakka, Y. Kawazoe, Adv. Funct. Mater. 23 (2013) 2185–2192.
[21] S.-Y. Pang, Y.-T. Wong, S. Yuan, Y. Liu, M.-K. Tsang, Z. Yang, H. Huang, W.-T. Wong, J. Hao, J. Am. Chem. Soc. 141 (2019) 9610–9616.
[22] M. Li, J. Lu, K. Luo, Y. Li, K. Chang, K. Chen, J. Zhou, J. Rosen, L. Hultman, P. Eklund, J. Am. Chem. Soc. 141 (2019) 4730–4737.
[23] V. Kamysbayev, A.S. Filatov, H. Hu, X. Rui, F. Lagunas, D. Wang, R.F. Klie, D.V. Talapin, Science 369 (2020) 979–983.
[24] Q. Tang, Z. Zhou, P. Shen, J. Am. Chem. Soc. 134 (2012) 16909–16916.
[25] C. Eames, M.S. Islam, J. Am. Chem. Soc. 136 (2014) 16270–16276.
[26] Y. Li, H. Shao, Z. Lin, J. Lu, L. Liu, B. Duployer, P.O. Persson, P. Eklund, L. Hultman, M. Li, Nat. Mater. 19 (2020) 894–899.
[27] M. Li, X. Li, G. Qin, K. Luo, J. Lu, Y. Li, G. Liang, Z. Huang, J. Zhou, L. Hultman ACS Nano 15 (2021) 1077–1085.
[28] P. Liu, W. Ding, J. Liu, L. Shen, F. Jiang, P. Liu, Z. Zhu, G. Zhang, C. Liu, J. Xu, J. Alloy. Compd. 829 (2020) 154634.
[29] S. Liu, K. He, X. Wu, X. Luo, B. Li, RSC Adv. 5 (2015) 87266–87276.
[30] Q. Peng, J. Guo, Q. Zhang, J. Xiang, B. Liu, A. Zhou, R. Liu, Y. Tian, J. Am. Chem. Soc. 136 (2014) 4113–4116.
[31] X. Zhang, Y. Liu, S. Dong, J. Yang, X. Liu, Electrochim. Acta 294 (2019) 233–239.
[32] G. Li, B.C. Wyatt, F. Song, C. Yu, Z. Wu, X. Xie, B. Anasori, N. Zhang, Adv. Funct. Mater. 31 (2021) 2105043.
[33] S. Venkateshalu, A.N. Grace, App. Mater. Today 18 (2020) 100509.
[34] H. Wang, J.-M. Lee, J. Mater. Chem. A 8 (2020) 10604–10624.
[35] M.A. Hope, A.C. Forse, K.J. Griffith, M.R. Lukatskaya, M. Ghidiu, Y. Gogotsi, C.P. Grey, Phys. Chem. Chem. Phys. 18 (2016) 5099–5102.
[36] M. Magnuson, L.-Å. Näslund, Phys. Rev. Res. 2 (2020) 033516.
[37] C. Shi, M. Beidaghi, M. Naguib, O. Mashtalir, Y. Gogotsi, S.J. Billinge, Phys. Rev. Lett. 112 (2014) 125501.
[38] D. Geng, X. Zhao, L. Li, P. Song, B. Tian, W. Liu, J. Chen, D. Shi, M. Lin, W. Zhou, 2D Mater. 4 (2016) 011012.
[39] M. Khazaei, M. Arai, T. Sasaki, A. Ranjbar, Y. Liang, S. Yunoki, Phys. Rev. B 92 (2015) 075411.
[40] T. Hu, Z. Li, M. Hu, J. Wang, Q. Hu, Q. Li, X. Wang, J. Phys. Chem C 121 (2017) 19254–19261.
[41] X. Sang, Y. Xie, D.E. Yilmaz, R. Lotfi, M. Alhabeb, A. Ostadhossein, B. Anasori, W. Sun, X. Li, K. Xiao, Nat. Commun. 9 (2018) 1–9.
[42] A. Enyashin, A. Ivanovskii, J. Solid State Chem. 207 (2013) 42–48.
[43] Q. Meng, J. Ma, Y. Zhang, Z. Li, C. Zhi, A. Hu, J. Fan, Nanoscale 10 (2018) 3385–3392.
[44] J. Zhou, X.-H. Zha, M. Yildizhan, P. Eklund, J. Xue, M. Liao, P.O. Persson, S. Du, Q. Huang, ACS Nano 13 (2019) 1195–1203.
[45] Z. Lin, S.R. Denny, J.G. Chen, J. Catal. 404 (2021) 929–942.
[46] X. Li, Y. Bai, X. Shi, N. Su, G. Nie, R. Zhang, H. Nie, L. Ye, Mater. Adv. 2 (2021) 1570–1594.
[47] S. Kumar, M.A. Rehman, S. Lee, M. Kim, H. Hong, J.-Y. Park, Y. Seo, Sci. Report. 11 (2021) 1–9.
[48] P. Forouzandeh, S.C. Pillai, Curr. Opin. Chem. Eng. 33 (2021) 100710.
[49] G. Li, S. Lian, F. Song, S. Chen, Z. Wu, X. Xie, N. Zhang, Small 17 (2021) 2103626.
[50] S. Hofmann, Springer Science + Business Media, Wilmersdorf, 2012 (2012).
[51] M. Benchakar, L. Loupias, C. Garnero, T. Bilyk, C. Morais, C. Canaff, N. Guignard, S. Morisset, H. Pazniak, S. Hurand, App. Surface Sci. 530 (2020) 147209.
[52] I. Persson, L.-Å. Näslund, J. Halim, M.W. Barsoum, V. Darakchieva, J. Palisaitis, J. Rosen, P.O.Å. Persson, 2D Mater 5 (2017) 015002.
[53] T. Schultz, N.C. Frey, K. Hantanasirisakul, S. Park, S.J. May, V.B. Shenoy, Y. Gogotsi, N. Koch, Chem. Mater. 31 (2019) 6590–6597.
[54] A. Lipatov, M. Alhabeb, M.R. Lukatskaya, A. Boson, Y. Gogotsi, A. Sinitskii, Adv. Electronic Mater. 2 (2016) 1600255.
[55] M. Ghidiu, M.R. Lukatskaya, M.-Q. Zhao, Y. Gogotsi, M.W. Barsoum, Nature 516 (2014) 78–81.
[56] X. Wang, C. Garnero, G. Rochard, D. Magne, S. Morisset, S. Hurand, P. Chartier, J. Rousseau, T. Cabioc'h, C. Coutanceau, J. Mater. Chem. A 5 (2017) (2023) 22012–22022.
[57] M. Wu, B. Wang, Q. Hu, L. Wang, A. Zhou Mater. 11 (2018) 2112.
[58] F. Du, H. Tang, L. Pan, T. Zhang, H. Lu, J. Xiong, J. Yang, C.J. Zhang, Electrochim. Acta 235 (2017) 690–699.
[59] O. Mashtalir, M.R. Lukatskaya, M.Q. Zhao, M.W. Barsoum, Y. Gogotsi, Adv. Mater. 27 (2015) 3501–3506.
[60] B. Anasori, M. Dahlqvist, J. Halim, E.J. Moon, J. Lu, B.C. Hosler, E.a.N. Caspi, S.J. May, L. Hultman, P. Eklund, J. App. Phys. 118 (2015) 094304.
[61] A. Pan, X. Ma, S. Huang, Y. Wu, M. Jia, Y. Shi, Y. Liu, P. Wangyang, L. He, Y. Liu, J. Phys. Chem. Lett. 10 (2019) 6590–6597.
[62] J. Yang, M. Naguib, M. Ghidiu, L.M. Pan, J. Gu, J. Nanda, J. Halim, Y. Gogotsi, M. W. Barsoum, J. Am. Chem. Soc. 99 (2016) 660–666.
[63] J. Zhou, X. Zha, F.Y. Chen, Q. Ye, P. Eklund, S. Du, Q. Huang, Angew. Chem. Int. Ed. 55 (2016) 5008–5013.
[64] W. Sun, S. Shah, Y. Chen, Z. Tan, H. Gao, T. Habib, M. Radovic, M. Green, J. Mater. Chem. A 5 (2017) 21663–21668.
[65] S. Yang, P. Zhang, F. Wang, A.G. Ricciardulli, M.R. Lohe, P.W. Blom, X. Feng, Angew Chem. 130 (2018) 15717–15721.
[66] H. Shi, P. Zhang, Z. Liu, S. Park, M.R. Lohe, Y. Wu, A. Shaygan Nia, S. Yang, X. Feng, Angew Chem. Int. Ed. 60 (2021) 8689–8693.
[67] X. Xie, Y. Xue, L. Li, S. Chen, Y. Nie, W. Ding, Z. Wei, Nanoscale 6 (2014) 11035–11040.
[68] G. Li, L. Tan, Y. Zhang, B. Wu, L. Li, Langmuir 33 (2017) 9000–9006.
[69] T. Li, L. Yao, Q. Liu, J. Gu, R. Luo, J. Li, X. Yan, W. Wang, P. Liu, B. Chen, Angew. Chem. Int. Ed. 57 (2018) 6115–6119.
[70] G. Zou, J. Guo, X. Liu, Q. Zhang, G. Huang, C. Fernandez, Q. Peng, Adv. Energy Mater. 7 (2017) 1700700.
[71] K.J. MacKenzie, M.E. Smith, Multinuclear Solid State Nuclear Magnetic Resonance of Materials., Pergamon Press, Oxford (2002).
[72] S. Hartmann, E. Hahn, Phy. Rev. 128 (1962) 2042.
[73] K.J. Harris, M. Bugnet, M. Naguib, M.W. Barsoum, G.R. Goward, J. Phys. Chem. C 119 (2015) 13713–13720.
[74] T. Hu, J. Wang, H. Zhang, Z. Li, M. Hu, X. Wang, Phys. Chem. Chem. Phys. 17 (2015) 9997–10003.
[75] T. Hu, M. Hu, B. Gao, W. Li, X. Wang, J. Phys. Chem. C 122 (2018) 18501–18509.
[76] D.B. Lioi, G. Neher, J.E. Heckler, T. Back, F. Mehmood, D. Nepal, R. Pachter, R. Vaia, W.J. Kennedy, , Mater. 2 (2019) 6087–6091.
[77] T. Hu, M. Hu, Z. Li, H. Zhang, C. Zhang, J. Wang, X. Wang, J. Phys. Chem. A 119 (2015) 12977–12984.
[78] A. Sarycheva, Y. Gogotsi, Chem. Mater. 32 (2020) 3480–3488.
[79] M. Alhabeb, K. Maleski, B. Anasori, P. Lelyukh, L. Clark, S. Sin, Y. Gogotsi, Chem. Mater. 29 (2017) 7633–7644.
[80] M.R. Lukatskaya, S.M. Bak, X. Yu, X.Q. Yang, M.W. Barsoum, Y. Gogotsi, Adv. Energy Mater. 5 (2015) 1500589.
[81] Z. Li, L. Yu, C. Milligan, T. Ma, L. Zhou, Y. Cui, Z. Qi, N. Libretto, B. Xu, J. Luo Nat. Commun. 9 (2018) 1–8.
[82] D. Zhao, Z. Chen, W. Yang, S. Liu, X. Zhang, Y. Yu, W.-C. Cheong, L. Zheng, F. Ren, G. Ying, J. Am. Chem. Soc. 141 (2019) 4086–4093.
[83] N. Jiang, D. Su, J. Spence, Phys. Chem. B 76 (2007) 214117.
[84] Y. Qin, X.-H. Zha, X. Bai, K. Luo, Q. Huang, Y. Wang, S. Du, J. Phys.: Condens. Matter 32 (2020) 135302.
[85] X.-H. Zha, K. Luo, Q. Li, Q. Huang, J. He, X. Wen, S. Du, Europhys. Lett. 111 (2015) 26007.
[86] L.-Å. Näslund, M.-H. Mikkelä, E. Kokkonen, M. Magnuson, 2D Mater 8 (2021) 045026.
[87] P.O. Persson, J. Rosen, Curr. Opin. Solid State Mater Sci. 23 (2019) 100774.
[88] G. Lu, S.L. Bernasek, J. Schwartz, Surface Sci. 458 (2000) 80–90.
[89] Y.G. Gogotsi, R.A. Andrievski, Springer Science + Business Media, Berlin (2012).
[90] C.J. Zhang, S. Pinilla, N. McEvoy, C.P. Cullen, B. Anasori, E. Long, S.-H. Park, A.S. Seral-Ascaso, A. Shmeliov, D. Krishnan, Chem. Mater. 29 (2017) 4848–4856.
[91] O. Mashtalir, M.R. Lukatskaya, A.I. Kolesnikov, E. Raymundo-Pinero, M. Naguib, M. Barsoum, Y. Gogotsi, Nanoscale 8 (2016) 9128–9133.
[92] J. Come, J.M. Black, M.R. Lukatskaya, M. Naguib, M. Beidaghi, A.J. Rondinone, S. V. Kalinin, D.J. Wesolowski, Y. Gogotsi, N. Balke, Nano Energy 17 (2015) 27–35.
[93] L. Wang, W. Tao, L. Yuan, Z. Liu, Q. Huang, Z. Chai, J.K. Gibson, W. Shi, Chem. Commun. 53 (2017) 12084–12087.

[94] Y. Bai, K. Zhou, N. Srikanth, J.H. Pang, X. He, R. Wang, RSC Adv. 6 (2016) 35731–35739.
[95] K. Maleski, V.N. Mochalin, Y. Gogotsi, Chem. Mater. 29 (2017) 1632–1640.
[96] M. Khazaei, A. Ranjbar, M. Arai, T. Sasaki, S. Yunoki, J. Mater. Chem. C 5 (2017) 2488–2503.
[97] J. Guo, B. Legum, B. Anasori, K. Wang, P. Lelyukh, Y. Gogotsi, C.A. Randall, Adv. Mater. 30 (2018) 1801846.
[98] J.L. Hart, K. Hantanasirisakul, A.C. Lang, B. Anasori, D. Pinto, Y. Pivak, J.T. van Omme, S.J. May, Y. Gogotsi, M.L. Taheri, Nat. Commun. 10 (2019) 1–10.
[99] D. Magne, V. Mauchamp, S. Célérier, P. Chartier, T. Cabioc'h, Phys. Chem. Chem. Phys. 18 (2016) 30946–30953.
[100] J.L. Hart, A.C. Lang, A.C. Leff, P. Longo, C. Trevor, R.D. Twesten, M.L. Taheri, Sci. Report 7 (2017) 1–14.
[101] Y. Xie, P. Kent, Phys. Rev. B 87 (2013) 235441.
[102] Y.I. Jhon, J. Koo, B. Anasori, M. Seo, J.H. Lee, Y. Gogotsi, Y.M. Jhon, Adv. Mater. 29 (2017) 1702496.
[103] K. Wang, Y. Zhou, W. Xu, D. Huang, Z. Wang, M. Hong, Ceram. Int. 42 (2016) 8419–8424.
[104] H. Ghassemi, W. Harlow, O. Mashtalir, M. Beidaghi, M. Lukatskaya, Y. Gogotsi, M.L. Taheri, J. Mater. Chem. A 2 (2014) 14339–14343.
[105] B. Anasori, Y. Xie, M. Beidaghi, J. Lu, B.C. Hosler, L. Hultman, P.R. Kent, Y. Gogotsi, M.W. Barsoum, ACS Nano 9 (2015) 9507–9516.
[106] B. Anasori, C. Shi, E.J. Moon, Y. Xie, C.A. Voigt, P.R. Kent, S.J. May, S.J. Billinge, M.W. Barsoum, Y. Gogotsi, Nanoscale Horiz. 1 (2016) 227–234.
[107] G. Berdiyorov, Aip Adv. 6 (2016) 055105.
[108] M. Khazaei, M. Arai, T. Sasaki, M. Estili, Y. Sakka, Phys. Chem. Chem. Phys. 16 (2014) 7841–7849.
[109] A.N. Enyashin, A.L. Ivanovskii, J. Phys. Chem. C 117 (2013) 13637–13643.
[110] A. Champagne, L. Shi, T. Ouisse, B. Hackens, J.-C. Charlier, Phys. Rev. B 97 (2018) 115439.
[111] L. Dong, H. Kumar, B. Anasori, Y. Gogotsi, V.B. Shenoy, J. Phys. Chem. Lett. 8 (2017) 422–428.
[112] E.M. Siriwardane, D. Çakir, J. App. Phys. 125 (2019) 082527.
[113] A. Iqbal, J. Kwon, M.-K. Kim, C. Koo, Mater. Today Adv. 9 (2021) 100124.
[114] Y. Lee, Y. Hwang, Y.-C. Chung, ACS App. Mater Interf. 7 (2015) 7163–7169.
[115] G. Gao, G. Ding, J. Li, K. Yao, M. Wu, M. Qian, Nanoscale 8 (2016) 8986–8994.
[116] J. Lei, A. Kutana, B.I. Yakobson, J. Mater. Chem. C 5 (2017) 3438–3444.
[117] J. Halim, M.R. Lukatskaya, K.M. Cook, J. Lu, C.R. Smith, L.-Å. Näslund, S.J. May, L. Hultman, Y. Gogotsi, P. Eklund, Chem. Mater. 26 (2014) 2374–2381.
[118] Y. Dong, S.S.K. Mallineni, K. Maleski, H. Behlow, V.N. Mochalin, A.M. Rao, Y. Gogotsi, R. Podila, Nano Energy 44 (2018) 103–110.
[119] M. Han, C.E. Shuck, R. Rakhmanov, D. Parchment, B. Anasori, C.M. Koo, G. Friedman, Y. Gogotsi, ACS Nano 14 (2020) 5008–5016.
[120] S. Huang, V.N. Mochalin, Inorg. Chem. 58 (2019) 1958–1966.
[121] A. Avgustinik, G. Drozdetskaya, S. Ordan'yan, Soviet Powder Metallurgy Metal Ceram. 6 (1967) 470–473.
[122] X. Zhao, A. Vashisth, E. Prehn, W. Sun, S.A. Shah, T. Habib, Y. Chen, Z. Tan, J.L. Lutkenhaus, M. Radovic, Matter 1 (2019) 513–526.
[123] M. Naguib, O. Mashtalir, M.R. Lukatskaya, B. Dyatkin, C. Zhang, V. Presser, Y. Gogotsi, M.W. Barsoum, Chem. Commun. 50 (2014) 7420–7423.
[124] S. Huang, V.N. Mochalin, ACS Nano 14 (2020) 10251–10257.
[125] C. Wang, Y.-L. Pan, S.C. Hill, B. Redding, J. Quant. Spectrosc. Ra.Trans. 153 (2015) 4–12.
[126] Z. Du, X. Zhang, S. Xi, L. Li, Z. Luan, C. Lian, B. Wang, J. Yan, J. Asian Earth Sci. 168 (2018) 197–206.
[127] O. Mashtalir, K.M. Cook, V.N. Mochalin, M. Crowe, M.W. Barsoum, Y. Gogotsi, J. Mater. Chem. A 2 (2014) 14334–14338.
[128] J. Halim, K.M. Cook, M. Naguib, P. Eklund, Y. Gogotsi, J. Rosen, M.W. Barsoum, App Surface Sci. 362 (2016) 406–417.
[129] V. Natu, R. Pai, M. Sokol, M. Carey, V. Kalra, M.W. Barsoum, Chem 6 (2020) 616–630.
[130] G. Greczynski, L. Hultman, ChemPhysChem 18 (2017) 1507.
[131] M. Anthony, M. Seah, Surface Interf. ANALY. 6 (1984) 107–115.